Refrustration and competing orders in the prototypical $Dy_2Ti_2O_7$ spin ice material

P. Henelius,[1,*] T. Lin,[2] M. Enjalran,[3,4] Z. Hao,[2] J. G. Rau,[2] J. Altosaar,[2,5] F. Flicker,[6] T. Yavors'kii,[7] and M. J. P. Gingras[2,8,9]

[1]*Department of Theoretical Physics, Royal Institute of Technology, SE-106 91 Stockholm, Sweden*

[2]*Department of Physics and Astronomy, University of Waterloo, Waterloo, Ontario, Canada N2L 3G1*

[3]*Department of Physics, Southern Connecticut State University, 501 Crescent Street, New Haven, Connecticut 06515-1355, USA*

[4]*Connecticut State Colleges and Universities Center for Nanotechnology, Southern Connecticut State University, New Haven, Connecticut 06515-1355, USA*

[5]*Department of Physics, Princeton University, Princeton, New Jersey 08544, USA*

[6]*Department of Physics, University of California, Berkeley, California 94720, USA*

[7]*Applied Mathematics Research Centre, Coventry University, Coventry, CV1 5FB, United Kingdom*

[8]*Canadian Institute for Advanced Research, 180 Dundas St. W., Toronto, Ontario, Canada M5G 1Z8*

[9]*Perimeter Institute for Theoretical Physics, 31 Caroline St. N., Waterloo, Ontario, Canada N2L 2Y5*

(Received 12 July 2015; published 7 January 2016)

Spin ices, frustrated magnetic materials analogous to common water ice, have emerged over the past 15 years as exemplars of high frustration in three dimensions. Recent experimental developments aimed at interrogating anew the low-temperature properties of these systems, in particular whether the predicted transition to long-range order occurs, behoove researchers to scrutinize our current dipolar spin ice model description of these materials. In this work, we do so by combining extensive Monte Carlo simulations and mean-field theory calculations to analyze data from previous magnetization, diffuse neutron scattering, and specific-heat measurements on the paradigmatic $Dy_2Ti_2O_7$ spin ice material. In this work, we also reconsider the possible importance of the nuclear specific heat $C_{\rm nuc}$ in $Dy_2Ti_2O_7$. We find that $C_{\rm nuc}$ is not entirely negligible below a temperature $\sim$0.5 K and must therefore be taken into account in a quantitative analysis of the calorimetric data of this compound below that temperature. We find that in this material, small effective spin-spin exchange interactions compete with the magnetostatic dipolar interaction responsible for the main spin ice phenomenology. This causes an unexpected "refrustration" of the long-range order that would be expected from the incompletely self-screened dipolar interaction and which positions the material at the boundary between two competing classical long-range-ordered ground states. This allows for the manifestation of new physical low-temperature phenomena in $Dy_2Ti_2O_7$, as exposed by recent specific-heat measurements. We show that among the four most likely causes for the observed upturn of the specific heat at low temperature [an exchange-induced transition to long-range order, quantum non-Ising (transverse) terms in the effective spin Hamiltonian, the nuclear hyperfine contribution, and random disorder], only the last appears to be reasonably able to explain the calorimetric data.

DOI: 10.1103/PhysRevB.93.024402

I. INTRODUCTION

Highly frustrated magnetism (HFM) arises when the leading effective spin-spin interactions are in strong competition among themselves [1–3]. High frustration dramatically weakens a material's tendency towards conventional long-range magnetic order. This opens up an avenue to the discovery of spin liquids, intriguing states of matter where the magnetic degrees of freedom are disordered by quantum mechanical fluctuations even at absolute zero temperature [3–5]. It is convenient to follow Anderson's perspective [4] and divide models of HFM into two classes. In the first, the lattice architecture frustrates the predominant antiferromagnetic (AF) nearest-neighbor interactions and the formation of a unique collinear long-range-ordered Néel state. Popular examples of such highly frustrated lattice structures include the kagome and pyrochlore lattices in two and three dimensions, respectively [1,3,5]. In the second class, one finds a number of interactions of roughly the same scale that compete to control the development of distinct magnetic correlations. A well-known example of this second class is the J_1-J_2 model on the square lattice [4,6–8]. More recently, it has been suggested that frustration based on competing interactions, as opposed to the common geometrical antiferromagnetic nearest-neighbor frustration, is at play in the kagome-based antiferromagnetic kappellasite material [9].

The first class of HFM systems has attracted the most attention from experimentalists because, unlike the second class, it does not rely on a fine-tuning accident of nature (e.g., $J_2 \sim J_1/2$ in the J_1-J_2 model [6]) to be at a strong frustration point to induce large quantum spin fluctuations. In this class, there is no unique long-range-ordered state selected at the mean-field level and the spectrum of soft modes is dispersionless throughout the whole Brillouin zone [10–12]. Consequently, these systems are very soft even at the classical level and show limited propensity towards ordering [13], suggesting that magnetic materials involving such lattices are attractive candidates in the search for a spin liquid state [3,5]. High frustration does not only enable large thermal and quantum fluctuations. It also allows for random disorder, in the form of off-stoichiometry or intersite mixing, for example, to have dramatic effects on the low-temperature properties of a system [13,14].

Spin ices, in which the magnetic moments obey an energetic "ice rule" similar to that governing the proton positions in

*henelius@kth.se

common water ice [15,16], have traditionally been viewed as belonging to the first category of HFM systems [2,12,15,16]. The two textbook examples of spin ice materials are the rare-earth pyrochlore oxides $Ho_2Ti_2O_7$ (Ref. [17]) and $Dy_2Ti_2O_7$ (Ref. [18]) in which Ho^{3+} and Dy^{3+} are the magnetic ions. The key signature of spin ices [the formation of an exponentially large number of nearly degenerate low-energy states (called the spin ice manifold) at sufficiently low temperature T] does not require fine tuning [12]. Indeed, the spin ice phenomenon is robust and consistent with the two dominant spin-spin interactions: the nearest-neighbor exchange J_1 and the long-range dipolar interactions of strength D. However, in this J_1-D dipolar spin ice model (DSM) [19,20], the imperfect screening of the magnetostatic dipolar $1/r^3$ tail [12,21] is theoretically expected to induce a transition to long-range order at $T \approx 0.13D$ as found in Monte Carlo simulations [22,23]. Experiments [17,18,24,25], on the other hand, have so far not found evidence for a transition to long-range order. It has generally been assumed that this is the result of the dynamical arrest and freezing out of gapped spin-flip excitations ("monopoles") [26] at low temperatures [27,28], as made clear by recent experiments aimed at studying the low-temperature dynamical and thermodynamical properties of spin ices [28–31]. It is therefore surprising and noteworthy that one of these experiments on $Dy_2Ti_2O_7$ (Ref. [30]) finds an *increase* in the magnetic specific heat $C(T)$ below a temperature $T^* \sim 0.5$ K, as opposed to a rapid plunge of $C(T)$ to zero around that temperature as found in all previous specific-heat measurements on this compound [18,32–34]. The rise of $C(T)$ observed in Ref. [30] results in a concurrent continuous decrease of the thermal magnetic entropy with no signature of a residual Pauling entropy plateau over any extended temperature window. Moreover, this observed rise in $C(T)$ is not in accord with the predictions of the original DSM [20,22,23] or its refinement [35,36] that includes long-range dipolar interactions as well as exchange interactions up to third-nearest neighbor. Given the successes of this refined DSM [35,36] in rationalizing a number of experimental aspects of $Dy_2Ti_2O_7$, the results of Ref. [30] beg the question that motivated this study: "What is the microscopic origin of the observed rise in $C(T)$ for $T \lesssim 0.5$ K?"

This is an important question because the $C(T)$ upturn could suggest some heretofore unexposed physics going on deep in the low-temperature spin ice regime of $Dy_2Ti_2O_7$. For example, this upturn could signal the emergence of quantum effects and suggest that the previously assumed strictly classical [15] $Dy_2Ti_2O_7$ spin ice may be in fact entering a quantum spin ice state at sufficiently low temperature, thus offering itself as an unexpected realization of a quantum spin liquid [5].

To address the above question, we step all the way back to reassess the premises defining the spin-spin couplings of the DSM [20,35,36] and discuss what we consider the most cogent way to proceed. In the $Dy_2Ti_2O_7$ and $Ho_2Ti_2O_7$ dipolar spin ice materials, the spin ice regime is a collective paramagnetic state [13], a classical spin liquid of sorts [3]. In that liquid regime, the thermal evolution of most thermodynamic quantities is smooth and without sharp features (e.g., specific heat). This is the reason why the temperature and magnetic field dependence of several quantities need to be simultaneously fitted to parametrize the spin-spin coupling of the DSM beyond the nearest-neighbor exchange. This problem did not arise in the formulation of the simplest original DSM [20] which contains only one independent (nearest-neighbor) exchange coupling. This exchange could be determined by fitting independently the temperature at which the specific heat peaks or the height of that peak since the dipolar strength D is *a priori* known from the saturation magnetization of the material and the lattice spacing. Such a fitting of multiple thermodynamic quantities is the procedure that was followed in Ref. [36]. An important conclusion of that study was that the so-determined Hamiltonian would most likely display a transition to long-range order near 100 mK. This prediction would seem to be in significant disagreement with the recent experiment of Pomaranski *et al.* [30] if the upturn of the specific heat at $T \sim 0.5$ K were to be interpreted as a harbinger of an impending transition to long-range order.

In this work, we follow an approach that differs in two ways from the work of Ref. [36]. First of all, we consider an experiment on $Dy_2Ti_2O_7$ [37–39] performed with a magnetic field applied along a direction such that one can invoke symmetry considerations and settings that allow us to determine two symmetry-distinct subleading (third-nearest-neighbor) exchange parameters that would be difficult to determine from measurements that do not exploit such an astute experimental symmetry setup. Second, as spin-spin correlations, and therefore their reciprocal space description as probed by neutron scattering, are the observables most directly linked to the details of the spin Hamiltonian, we scrutinize the reciprocal space details of a neutron scattering intensity map previously obtained on $Dy_2Ti_2O_7$ spin ice [40].

By comparing detailed experimental information on the spin-spin correlations contained in neutron scattering results on $Dy_2Ti_2O_7$ with that of Monte Carlo simulations, we show in the following that the best set of couplings parametrizing its spin Hamiltonian positions $Dy_2Ti_2O_7$ near the phase boundary between two competing classical long-range-ordered spin ice states. We find that the recovery of the Pauling entropy is a more intricate process than previously thought, with the boundary region rich in unusual phenomena such as a nearly energetically degenerate stacking of ordered spin planes. Through a remarkable coincidence of nature, the competing distance-dependent exchange and dipolar interactions in $Dy_2Ti_2O_7$ "refrustrate" this material at low temperature[1] and, therefore, make it a new example of the second class of HFM systems discussed above.

Such a competition between various classical ground states may in principle allow for an enhanced level of quantum fluctuations and contribute to driving dipolar spin ices, traditionally viewed as strictly classical Ising systems [15], into a U(1) quantum spin liquid state [5,41]. This is reminiscent of the J_1-J_2 model at the $J_2 = J_1/2$ point where two classical ground states are also degenerate [6]. Because the critical

[1]By "refrustrate" we mean that exchange interactions beyond nearest neighbor compete with the meager tendency of the long-range part of the dipolar interactions to lift the degeneracy of the ice-rule states [12,21] with an associated transition at a temperature $T_c \sim 0.13D$ [22,23] and further depress the ordering transition to an even lower temperature.

transition temperature for the exchange parameters determined from the analysis of the neutron scattering data is far below the upturn seen in the specific-heat data [30], we are unable to describe the $C(T)$ data of Ref. [30] for $T \lesssim 0.7$ K with those parameters, even after accounting for the non-negligible nuclear contribution to the total specific heat below that temperature. This leads us to reconsider how strong the heretofore largely ignored quantum (non-Ising) terms in the Hamiltonian may be for $Dy_2Ti_2O_7$ (see, however, Ref. [41] for a study that does consider possible quantum effects). Motivated by recent works having found that various forms of random disorder are present in magnetic rare-earth pyrochlore oxides [31,42,43], we also explore what effect random disorder may have on the low-temperature properties of this material. We reaffirm that the quantum terms in $Dy_2Ti_2O_7$ should be very small indeed and unlikely to be responsible for the development of a low-temperature quantum coherence (e.g., coherent hopping of spinons [44], i.e., spin ice monopoles [26]) that would be signaled by a rise in $C(T)$, similarly to that recently reported in a quantum Monte Carlo simulation study of a quantum spin ice model [45]. On the other hand, we show that random disorder, in the form of intersite disorder [42,43] (e.g., "stuffing"), could potentially explain the rise of $C(T)$ without dramatically affecting the neutron scattering intensity pattern over the same temperature range.

The rest of the paper is organized as follows. In Sec. II, we define the dipolar spin ice model that we study in this paper along with the Monte Carlo simulation that we employ to analyze the various experimental data that we consider. Section III contains the essential results of our work. Section III A presents the analysis of the [112] magnetic field magnetization measurements used to constrain the exchange parameters defining our dipolar spin ice model. Section III B discusses the long-range-ordered phases that the dipolar spin ice model displays within the constrained spin-spin coupling constants determined in Sec. III A. Section III C reports the analysis of previously published neutron scattering data on $Dy_2Ti_2O_7$ that allows us to position this compound in the phase diagram determined in Sec. III B. In Sec. III D, we analyze the recent specific-heat data in relation to the phase diagram presented in Sec. III B. In Sec. III E, we make a detailed comparison of the Monte Carlo results for the specific heat and neutron scattering intensity obtained in the distinct parts of the phase diagram and show that we are unable to reconcile the experimental specific-heat measurements of Ref. [30] with the spin-spin couplings identified in Sec. III B that describe the main features of the neutron scattering data. In Sec. III F, we argue that quantum (non-Ising) exchange couplings that one might want to consider in the dipolar spin ice model [41] are likely to be much too small to explain the upturn in the specific heat below a temperature of $T^* \sim 0.5$ K or so in $Dy_2Ti_2O_7$. On the other hand, the same subsection explores a toy model of random disorder (in the form of stuffed spins) that could possibly rationalize the specific-heat upturn. Finally, we close the paper with a brief conclusion in Sec. IV. With the aim of providing a streamlined reading of the key results presented in the main text, we have packaged all the technical details of the simulations, data analysis, and other calculations supporting the key results discussed in the main text in a series of appendixes.

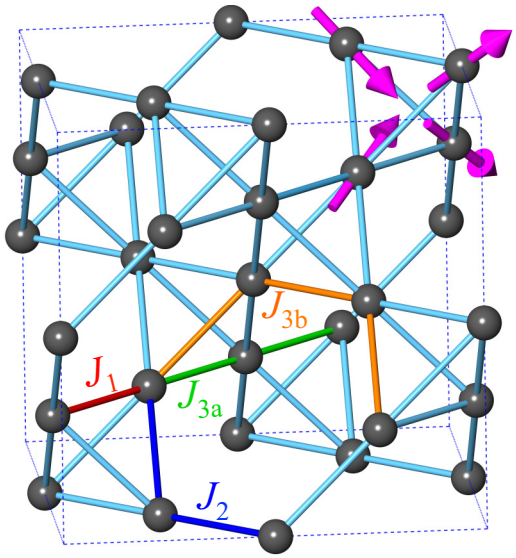

FIG. 1. Set of interacting neighbors on the pyrochlore lattice. The first- (J_1), second- (J_2), and two distinct third- (J_{3a} and J_{3b}) nearest-neighbor pathways are indicated by red, blue, green, and orange connections, respectively, on the pyrochlore lattice of corner-sharing tetrahedra. A two-in/two-out state of two spins pointing into the center of the tetrahedron and two spins pointing out from the tetrahedron is shown in the upper-right-hand corner of the lattice. An ice-rule obeying state is characterized by all tetrahedra being in a two-in/two-out spin configuration, but with no other constraint on the orientation of the spins.

II. MODEL AND MONTE CARLO METHOD

A. Model

In $Dy_2Ti_2O_7$, the magnetic Dy^{3+} rare-earth moments occupy the sites of the pyrochlore lattice shown in Fig. 1. This structure can be described as a face-centered-cubic (fcc) space lattice with a primitive basis that consists of a tetrahedron [2] (four sites). The microscopic Dy^{3+}–Dy^{3+} interionic magnetic and superexchange couplings are small ($[10^{-2}$–$10^{-1}]$ K) compared to the energy splitting ($\Delta \sim 300$ K) between the crystal-field ground-state doublet and the first-excited doublet [2]. One can thus project these interactions into a reduced Hilbert space comprised solely of the single-ion crystal-field ground states [15], ignoring for the moment unusually strong high-rank multipolar Dy-Dy interactions [46,47]. Due to the specific spectral decomposition of the crystal-field ground-state doublet [2,15], the effective (projected) Hamiltonian can then be expressed as a classical Ising model [15]. We return to this fundamental assumption in Sec. III F. The "spins" in that Ising model interact via distance-dependent "exchange" couplings J_{ij}, between ions i and j, as well as through the long-range magnetostatic dipole-dipole interaction. The Hamiltonian for this generalized dipolar spin ice model [20,22,35–37] (g-DSM) in an external magnetic field $\boldsymbol{H}$ reads as

$$\mathcal{H} = Dr_{\rm nn}^3 \sum_{i>j} \frac{\boldsymbol{S}_i \cdot \boldsymbol{S}_j}{|\boldsymbol{r}_{ij}|^3} - \frac{3(\boldsymbol{S}_i \cdot \boldsymbol{r}_{ij})(\boldsymbol{S}_j \cdot \boldsymbol{r}_{ij})}{|\boldsymbol{r}_{ij}|^5} + \sum_{i>j} J_{ij} \boldsymbol{S}_i \cdot \boldsymbol{S}_j - g\mu_B \langle J^z \rangle \sum_i \boldsymbol{S} \cdot \boldsymbol{H}. \quad (1)$$

The scale of the dipolar interaction at the nearest-neighbor distance $r_{\rm nn}$ is given by $D = \mu_0(g\mu_B\langle J^z\rangle)^2/4\pi r_{\rm nn}^3 = 1.3224$ K (Ref. [36]) using $\langle J^z\rangle = 7.40$ (Ref. [36]), $r_{\rm nn} = 3.58$ Å (Ref. [25]) and the Dy^{3+} Landé g factor is $g = \frac{4}{3}$. Here, $\boldsymbol{S}_i$ is a classical unit vector representing the Dy^{3+} magnetic moment at site i which is constrained by the crystal-field Ising anisotropy to point along the local $\hat{z}_i$ cubic [111] direction. We thus have $\boldsymbol{S}_i = \sigma_i\hat{z}_i$ with $\sigma_i = \pm 1$ as the Ising variable.[2] For sites i and j that belong to different sublattices $\hat{z}_i \cdot \hat{z}_j = -\frac{1}{3}$, while $\hat{z}_i \cdot \hat{z}_j = 1$ if they belong to the same sublattice. For most of our paper, we consider first- (J_1), second- (J_2), and two distinct third-nearest-neighbor interactions (J_{3a} and J_{3b}), but take J_4 into account to check the validity of our conclusions. The intersite connectivity defined by the J_1, J_2, J_{3a}, and J_{3b} couplings is illustrated in Fig. 1.

B. Monte Carlo method

For the most part of this paper, we employed Monte Carlo simulations to investigate the thermodynamic properties of the model defined by Eq. (1). In order to help interpret the Monte Carlo results, we also used in Appendix B conventional mean-field theory, formulated in reciprocal space, as described in Ref. [48].

The Monte Carlo calculations were performed with periodic boundary conditions and using the Ewald summation technique to handle the long-range dipolar interaction [23,48]. The systems simulated consisted of L^3 cubic unit cells each with 16 sites. Loop updates [22,23] were used when the single-spin-flip acceptance rate fell below 1%. In order to ease the investigation of the phase diagram discussed in Sec. III B, loop Monte Carlo simulations were further supplemented by the parallel tempering method [49] using 72 distinct temperatures distributed between 0.05 and 0.7 K.

The neutron scattering structure factor to be compared with experiments was calculated according to

$$S(\boldsymbol{q}) = \frac{[f(|\boldsymbol{q}|)]^2}{N}\sum_{ij}\langle s_i s_j\rangle(\hat{z}_i^{\perp}\cdot\hat{z}_j^{\perp})e^{i\boldsymbol{q}\cdot\boldsymbol{r}_{ij}}, \qquad (2)$$

where $\hat{z}_i^{\perp}$ is the component of the local Ising axis perpendicular to the wave vector $\boldsymbol{q}$ and $f(|\boldsymbol{q}|)$ is the magnetic form factor of Dy^{3+} (Ref. [50]). Points of particular interest are $\boldsymbol{q} = (0\,0\,3)$ and $\boldsymbol{q} = (\frac{3}{2}\ \frac{3}{2}\ \frac{3}{2})$ with $[f(|0\,0\,3|)]^2 = 0.8224$ and $[f(|\frac{3}{2}\ \frac{3}{2}\ \frac{3}{2}|)]^2 = 0.8627$.

In Sec. III F, we explore the effects of local effective magnetic degrees of freedom that may be generated by some form of random disorder such as stuffing (magnetic ions on the B site of the pyrochlore lattice, oxygen vacancies, or both). To do so, we consider a minimal *effective* impurity model that consists of impurity magnetic moments on the B sites of the pyrochlore lattice, termed "stuffed" spins [42].[3]

[2]Here, we have chosen to write the expected effective Ising exchange interactions for Dy^{3+} ions [47] as $\boldsymbol{S}_i \cdot \boldsymbol{S}_j$ in order to keep with the notation used in several previous works.

[3]Recent x-ray synchrotron work [43] has shown that a small percentage of rare-earth (RE) ions occupying ("stuffing") the B-site nominally occupied by the tetravalent transition-metal ion (e.g., Ti^{4+}) in the $RE_2Ti_2O_7$ pyrochlore oxides is quite common, and found to occur, for example, in $Ho_2Ti_2O_7$, $Er_2Ti_2O_7$, and $Yb_2Ti_2O_7$.

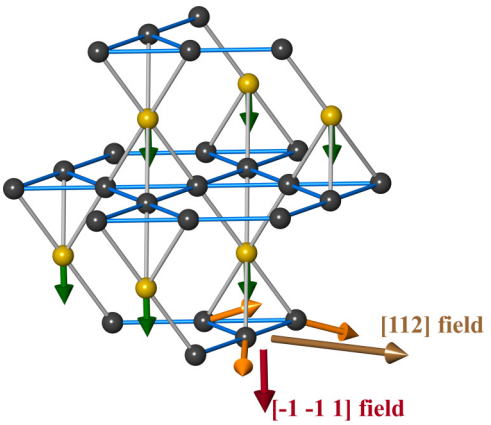

FIG. 2. Schematic illustration of the [112] field magnetization measurement with the structure of the pyrochlore lattice viewed as alternating triangular and kagome planes. An applied field in the [112] direction is shown as a brown arrow. An applied field along $[\bar{1}\bar{1}1]$ is shown in red. This field points along the local Ising axis of the green spin vectors on the triangular planes (yellow sites).

As a proof of principle, we assume for simplicity that the impurity spins are Ising type, with a local moment $\boldsymbol{L}_\alpha$ pointing along the line defined by the centers of the B-site tetrahedra on the pyrochlore lattice [2]. The stuffed spin $\boldsymbol{L}_\alpha$ is coupled to its six nearest neighbors $\boldsymbol{S}_i$ on the A sites with an effective exchange interaction

$$H_\Omega = -\Omega\sum_{\langle\alpha,i\rangle}\boldsymbol{L}_\alpha\cdot\boldsymbol{S}_i = \frac{\Omega}{3}\sigma_\alpha\sigma_i, \qquad (3)$$

where Ω is the coupling constant. Here, the index α runs over all randomly stuffed spins, which are chosen randomly to occupy a fraction p of the B sites, and $\sigma = \pm 1$.

III. RESULTS

A. [112] magnetic field experiment analysis

In this section, we begin to revisit the set of J_{ij} values describing $Dy_2Ti_2O_7$ and, unlike in other g-DSM works [35–37], we do not *a priori* assume that $J_{3a} = J_{3b}$. To do so, we first analyze magnetization data measured in a magnetic field near the [112] direction, with a small magnetic field component along $[\bar{1}\bar{1}1]$ (Ref. [38]). Figure 2 illustrates the geometry associated with this experiment. The analysis of this experiment allows us to establish constraints among the J_{ij} parameters and thus reduce the dimensionality of the model parameter space that needs to be explored to describe $Dy_2Ti_2O_7$.

This "[112] experiment" is rather remarkable in that it provides us with direct access to the third-nearest-neighbor interactions J_{3a} and J_{3b}. In this experiment, the large [112] component of the applied field saturates the magnetization on three of the four face-centered-cubic (fcc) sublattices that constitute the pyrochlore lattice. At the same time, a small

$[\bar{1}\bar{1}1]$ magnetic field component can be tuned so that the vector sum of the external applied plus the combined exchange and dipolar internal fields lead to a decoupling of the remaining fcc sublattice from the three fully polarized sublattices [37].

In Fig. 2, these decoupled magnetic moments reside on the triangular lattice indicated by the yellow sites with a downward green arrow. Since the nearest-neighbor distance on the fcc sublattice corresponds to the third-nearest-neighbor distance on the pyrochlore lattice, an analysis of the susceptibility for the field component along $[\bar{1}\bar{1}1]$ yields a relation between J_{3a} and J_{3b} that is almost linear and can be approximately described by (all in Kelvin),

$$J_{3b} = \begin{cases} -0.667 J_{3a} + 0.03 : & J_{3a} < 0.1, \\ -0.842 J_{3a} + 0.0474 : & J_{3a} > 0.1. \end{cases} \quad (4)$$

Furthermore, the applied experimental critical field in the $[\bar{1}\bar{1}1]$ direction that decouples the corresponding fcc sublattice from the internal ice rules, enforced by the combined exchange plus dipolar field, yields another linear relation between J_1 and J_2:

$$J_2 = -\tfrac{1}{2} J_1 + 1.555. \quad (5)$$

A derivation of these relations is given in Appendix A. In the following three subsections, we make use of the constraints defined by Eqs. (4) and (5) to analyze the ground state, spin-spin correlations, and associated neutron scattering function and thermodynamic properties of the model in the resulting J_1-J_{3a} parameter space.

B. Phase diagram

We now proceed to explore the phases and ordering wave vectors in the constrained J_1-J_{3a} parameter space where J_2 and J_{3b} have been eliminated via Eqs. (4) and (5). From extensive experimental and theoretical work, we know that $J_1 = 3.3 \pm 0.2$ K, and $|J_3| < 0.2$ K (Refs. [16,36]). Furthermore, work on the simple DSM with $J_2 = J_{3a} = J_{3b} = 0$ has shown [12,22] that, despite its highly frustrated nature, (reciprocal) $\boldsymbol{q}$-space mean-field theory [48] could be used to identify the candidate ordered state that ultimately develops if nonlocal loop dynamics are used to maintain equilibrium down to the ordering temperature [22,23]. By combining a mean-field theory survey of ordering wave vectors at the mean-field critical temperature with a direct analysis of the actual ordered states that appear in the Monte Carlo calculations (see Appendix B for details of the calculations), we find that there are two long-ranged-ordered ground states in the parameter range appropriate for $Dy_2Ti_2O_7$ (and as constrained by the [112] experimental results above). From the Monte Carlo results, the propagation vector of each ground state is (1 1 0) and $(\frac{1}{2}\ \frac{1}{2}\ 0)$. The first state was previously identified for the dipolar spin ice model with $J_2 = J_{3a} = J_{3b} = 0$ (Ref. [22]). In this state, parallel chains of spins order antiferromagnetically when viewed along a cubic $\langle 100 \rangle$ axis [see Fig. 13(a)]. We call this the "single-chain state." In the second state, pairs of adjacent spin chains are aligned, but each pair is antiparallel with the adjacent pairs and we refer to this as the "double-chain state" [see Fig. 13(b)]. The double-chain state is particularly interesting since the energy difference between different stackings in the z direction of the (001) plane of spins, shown in Fig. 13(c), is only $O(10^0)$ mK, and this state is thus quasidegenerate. Without the long-ranged dipolar interaction, different stackings have exactly the same (degenerate) energy. This is yet another manifestation of a self-screening effect emerging in spin ice [12,20,21]. This stacking degeneracy signals the "refrustration" of the DSM [20,22] alluded to in the title. It arises from the mutual competition of the (dimensionless) perturbative energy scales ($J_2/J_{\rm eff}$, $J_{3a}/J_{\rm eff}$, $J_{3b}/J_{\rm eff}$; $J_{\rm eff} \equiv [5D - J_1]/3$) (Refs. [16,20]) which mask the true ground-state order parameter at $\boldsymbol{q} = (\frac{1}{2}\ \frac{1}{2}\ 0)$. For example, the main intensity peak in $S(\boldsymbol{q})$ at a parameter point within the double-chain region at temperatures above the transition temperature appears at $\boldsymbol{q} = (\frac{1}{2}\ \frac{1}{2}\ \frac{1}{2})$, rather than at the ground-state order wave vector $\boldsymbol{q} = (\frac{1}{2}\ \frac{1}{2}\ 0)$. These results, which are reminiscent of the phenomenology at play in the three-dimensional ANNNI model [51], are further discussed in Appendix B.

To determine the phase boundary, we are prompted by the observation from the Monte Carlo simulations that the two ordered states are formed by ferromagnetically ordered spin chains. By considering these spin chains as the fundamental units of the system, we determine the following equation for the phase boundary:

$$J_{3a} + \frac{J_2}{3} + 0.02D = 0. \quad (6)$$

In the boundary region, phase competition increases the energy while *decreasing* the critical ordering temperature towards either ground state. This is explicitly demonstrated in Fig. 3, where the average energy is displayed as a function of temperature and J_{3a} as one crosses the boundary at $J_{3a} \cong 0.023$ K for $J_1 = 3.41$ K. While there is a clear first-order transition away from the boundary, it is much smoother at the boundary. The precise determination of the order of the phase transitions is beyond the scope of this work. Having determined the key candidate long-range-ordered phases for $Dy_2Ti_2O_7$, as well as the location of the phase boundary separating the competing ground states, we

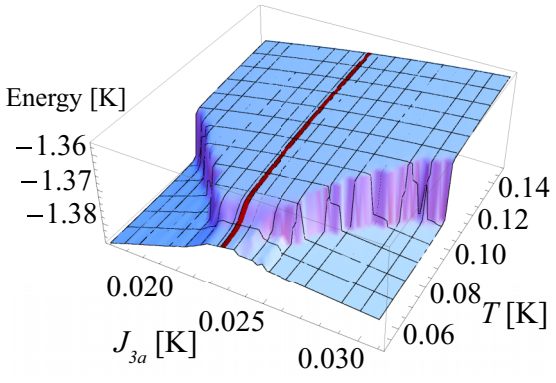

FIG. 3. The average thermal energy as a function of T and J_{3a} near the boundary between the single- and double-chain states for $J_1 = 3.41$ K. The phase boundary is located at $J_{3a} \approx 0.0228$ K and is marked by a red band. The phase transition is clearly first order away from the boundary, while the critical temperature is suppressed with the transition appearing to be close to continuous at the boundary.

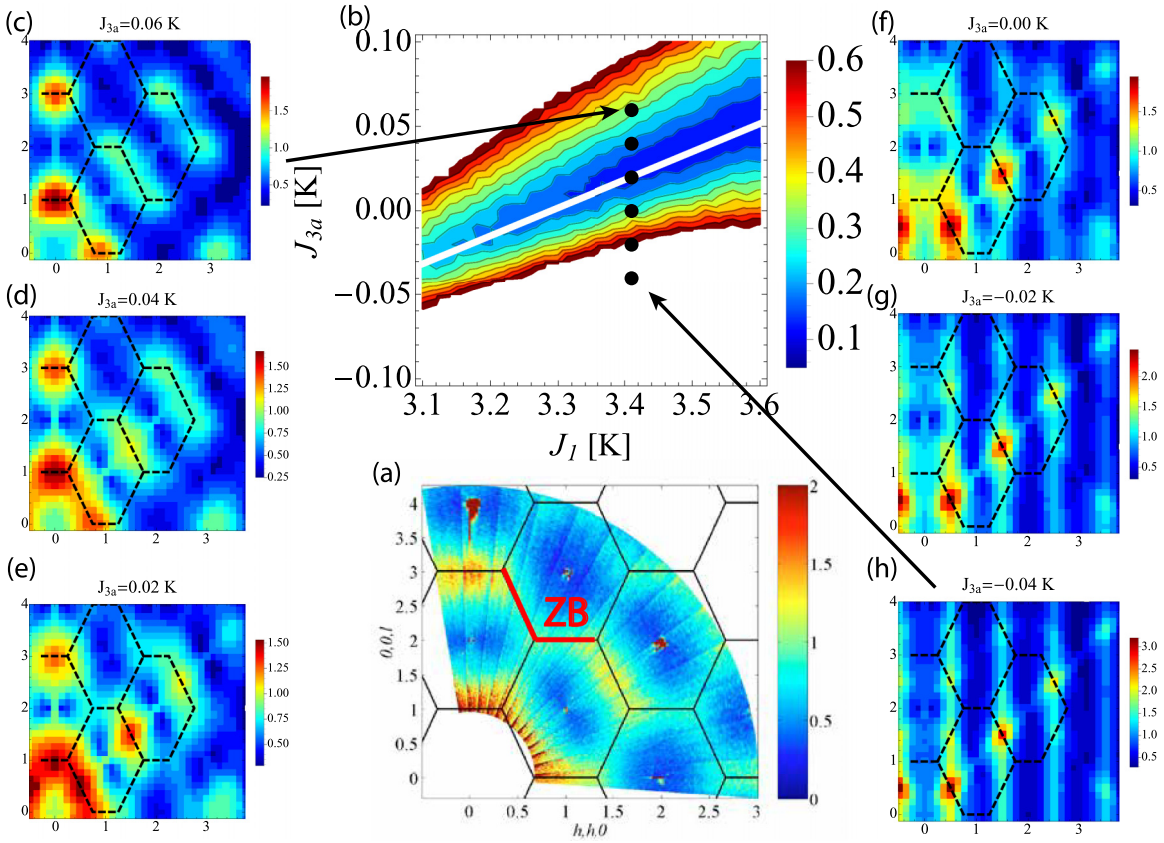

FIG. 4. Neutron structure factor and zone boundary scattering in the (hhl) plane across the phase boundary. (a) Experimental neutron scattering data at 0.3 K (Ref. [40]) with a section of the zone boundary (ZB) highlighted. (b) Deviation from constant scattering along the boundary segment ZB in the J_1-J_{3a} plane calculated through Monte Carlo simulations using Eq. (7). The phase boundary according to Eq. (6), in combination with Eq. (5), is shown as a white line. Note that the most "$\boldsymbol{q}$-space intensity-flat" ZBS (dark blue) is centered along the phase boundary. The corresponding value for the experimental data is $\sigma_{\mathrm{ZBS}} = 0.11$, in remarkably good agreement with the Monte Carlo result along the phase boundary. (c)–(h) Monte Carlo results for $S(\boldsymbol{q})$ in the vicinity of the single-chain (upper left region) to the double-chain transition (lower right region) for $J_1 = 3.41$ K at $T = 0.5$ K. The corresponding parameters in the J_1-J_{3a} space are marked by black dots. The intensity shifts from (0 0 3) to $(\frac{3}{2}\ \frac{3}{2}\ \frac{3}{2})$ as one crosses from the single-chain region (c) to the double-chain region (h).

now proceed to position this material within this parameter space.

C. Neutron scattering data analysis

As neutron scattering measurements provide direct information about the spin-spin correlations, an analysis of available neutron scattering data is a natural starting point for positioning $Dy_2Ti_2O_7$ in the J_1-J_{3a} phase diagram introduced in the previous subsection.

Before we begin presenting our results, we briefly comment on pinch-point singularities in the neutron scattering pattern of spin ice. The topic of pinch-point singularities in the equal-time (energy-integrated) neutron scattering data of spin ice had been the subject of much theoretical [21,52,53] and experimental [54–56] discussion. Pinch points in dipolar spin ice arise from the combination of the divergence-free condition of the coarse-grained magnetization field due to the two-in/two-out ice rules as well as the long-range dipole-dipole interaction [21,53], even at high temperature well above the formation of the spin ice manifold. As pinch points result from these two generic phenomenologies, they are not, apart from their ultimate disappearance [57], weighty signatures of the competing subleading exchange interactions beyond nearest neighbor that this study aims to expose. We therefore henceforth omit pinch points in our analysis and discussion of the neutron scattering data of $Dy_2Ti_2O_7$.

The main result of our analysis is shown in Fig. 4 where we consider the evolution of the neutron structure factor $S(\boldsymbol{q})$ upon crossing the single-/double-chain phase boundary and compare our numerical results to existing experimental data. We display in Fig. 4(a) the sub-Kelvin measurement of $S(\boldsymbol{q})$ reported in Ref. [40] and recorded at 0.3 K. We note two distinguishing features: pronounced peaks of roughly equal intensity at (0 0 3) and $(\frac{3}{2}\ \frac{3}{2}\ \frac{3}{2})$ and a ridge of rather flat scattering intensity spanning the Brillouin zone boundary. We refer to this feature as *zone-boundary scattering* (ZBS). The same fundamental features can also be discerned in the measurement recorded at 1.3 K in Ref. [40], but less clearly because of the weaker correlations at this higher temperature.

We first analyze the ZBS, whose defining signature observed here is a scattering intensity along the Brillouin zone boundary that is close to constant. A previous study [36] showed that ZBS in a dipolar spin ice, in particular $Dy_2Ti_2O_7$,

is an indication of competing Ising exchange interactions J_{ij} beyond nearest neighbor J_1, originally the only exchange coupling taken into account along with the long-range dipolar interactions in the DSM [20]. A similar phenomenology has been discussed in the context of the pyrochlore lattice with classical Heisenberg spins subject to beyond nearest-neighbor competing superexchange interactions [57].

As a quantitative measure of the ZBS feature in the Monte Carlo calculations, we use the deviation from flatness

$$\sigma^2_{\mathrm{ZBS}} = \frac{1}{N_q}\sum_{i=1}^{N_q}[S_{\mathrm{MC}}(q_i) - \langle S_{\mathrm{MC}}\rangle]^2, \tag{7}$$

along a zone-boundary (ZB) line segment indicated in the experimental neutron scattering in Fig. 4(a). The average of the scattering intensity along the segment is denoted $\langle S_{\mathrm{MC}}\rangle$ and the simulation was performed for a system size $L = 8$ with periodic boundary conditions, yielding $N_q = 9$ distinct $\boldsymbol{q}$ points on the zone boundary.

We display in Fig. 4(b) a color map of σ_{ZBS} in the constrained J_1-J_{3a} parameter space and note that the deviation from flatness is *smallest* along the phase boundary, indicating that flat ZBS is confined to the J_1-J_{3a} boundary region between the two competing ground states identified in Sec. III B.

The first main result of our study is that *only* in the vicinity of the phase boundary [white line in Fig. 4(b)] is there significant ZBS *as well as* peaks of roughly equal intensity at (0 0 3) and $(\frac{3}{2}\ \frac{3}{2}\ \frac{3}{2})$. These wave vectors, equivalent to (1 1 0) and $(\frac{1}{2}\ \frac{1}{2}\ \frac{1}{2})$ in the first Brillouin zone, are the main intensity peaks for the single- and double-chain states, respectively. This result can be deduced from Figs. 4(c)–4(h), where we display $S(\boldsymbol{q})$, calculated from Monte Carlo simulations, along a cut across the phase boundary (the solid white line) at $J_1 = 3.41$ K. Note that the peak at (0 0 3) is pronounced in the single-chain region above the phase boundary, while the peak at $(\frac{3}{2}\ \frac{3}{2}\ \frac{3}{2})$ dominates in the double-chain region below the boundary, as expected. Only in Figs. 4(d) and 4(e), close to the boundary, are the two peaks of similar intensity. Comparison with the experimental $S(\boldsymbol{q})$ data thus provides compelling evidence that the appropriate set of exchange parameters for $Dy_2Ti_2O_7$ puts the material quite close to the phase boundary between the single- and double-chain ground states. Note that this realization was much facilitated by the dimensional reduction of the J_{ij} parameter space using the above analysis of the [112] magnetization experiment in Sec. III A.

Considering the extraordinarily slow relaxation observed in experiments upon cooling [29,30], one could ask whether the neutron scattering data at 0.3 K are adequately equilibrated and therefore able to form the basis of a systematic analysis. It is therefore necessary to consider what effects a possible freezing of the sample may have on the properties of $S(\boldsymbol{q})$ that we consider here. In a Monte Carlo exploration of these effects, we find that there is *no* significant change in the ZBS and *no* fundamental reciprocal space redistribution in the peak intensities due to freezing. The details of the Monte Carlo results supporting this result are discussed in Appendix C. We therefore conclude that relative (0 0 3) and $(\frac{3}{2}\frac{3}{2}\frac{3}{2})$ peak intensities *and* ZBS in the experimental neutron scattering data place $Dy_2Ti_2O_7$ firmly near the boundary between the two competing states, *irrespective* of the possibility that the spin dynamics may have frozen at $T > 0.3$ K. Furthermore, and quite importantly, our analysis of the ratio of the peak intensity at (0 0 3) and $(\frac{3}{2}\ \frac{3}{2}\ \frac{3}{2})$ discussed in Appendix C reaches the very same conclusion *already* at $T = 1.3$ K, where $Dy_2Ti_2O_7$ has barely entered the spin ice regime and equilibration is not contentious.

D. Specific-heat analysis

The temperature dependence of the magnetic specific heat and, most importantly, the magnetic entropy, is one of the key indicators of the formation of the spin ice manifold. It is therefore necessary to consider how the recent specific-heat measurements [30] on $Dy_2Ti_2O_7$ fit in with the spin interaction model parametrized above to describe the main features of the neutron scattering pattern.

In the previous section we showed that neutron scattering data for $Dy_2Ti_2O_7$ are well described by the dipolar spin ice model with up to third-nearest-neighbor exchange. Our analysis of the neutron scattering data indicates that the material sits near the boundary between two ordered classical states and that our results are in good agreement with a previous analysis that did not rely on neutron scattering data [36]. On the boundary, we find that the system exhibits a Pauling entropy plateau for temperatures 200 mK $\lesssim T \lesssim$ 600 mK (see Fig. 9). In possible contradiction with this conclusion stands the recent specific-heat measurement employing very long equilibration time scales [30] which finds a rise of their raw $C_{\mathrm{raw}}(T)$ specific-heat data below the unexpectedly high temperature $T^* \sim 0.5$ K and a consequential lack of a Pauling entropy plateau. We investigate whether the specific-heat data can be modeled with our constrained J_1-J_{3a} parameter space. However, before proceeding to do so, we revisit what is the expected nuclear specific-heat contribution $C_{\mathrm{nuc}}(T)$ to the low-temperature ($T \lesssim 1$ K) specific-heat data reported in Ref. [30]. We then assess whether the results for the electronic specific heat (alone) are consistent with our conclusion based on our neutron scattering analysis.

1. Nuclear specific heat in $Dy_2Ti_2O_7$

$Dy_2Ti_2O_7$ and $Ho_2Ti_2O_7$ are the two prototypical dipolar spin ice materials. The latter, with its low neutron absorption cross section has been a favorite for neutron scattering studies [17,56,58]. On the other hand, the very large hyperfine contact interaction in Ho makes $Ho_2Ti_2O_7$ less attractive for specific-heat measurements, with the nuclear contribution to the specific heat overshadowing the electronic part for $T \lesssim 1.5$ K [58–60]. Conversely, $Dy_2Ti_2O_7$, because of the small hyperfine contact interaction of the only two nuclear spin-carrying ^{161}Dy and ^{163}Dy isotopes in $Dy_2Ti_2O_7$ with natural Dy isotope abundance, has generally been viewed as a much better suited compound for calorimetric measurements.

In their work, Pomaranski *et al.* [30] argued that the nuclear contribution to their (presumed) equilibrated specific-heat measurements down to 0.35 K is entirely negligible. To reach that conclusion, the authors of Ref. [30] referred to the nuclear specific heat $C_{\mathrm{nuc}}(T)$ estimated for the $Dy_3Ga_5O_{12}$ garnet in Ref. [61]. This estimation, transferred to $Dy_2Ti_2O_7$ using the high-temperature series expansion form for $C_{\mathrm{nuc}}(T)$ of Ref. [61] is quantitatively incorrect since the low-temperature static Dy^{3+} magnetic moment in $Dy_3Ga_5O_{12}$ is about $\sim$4.5 μ_B,

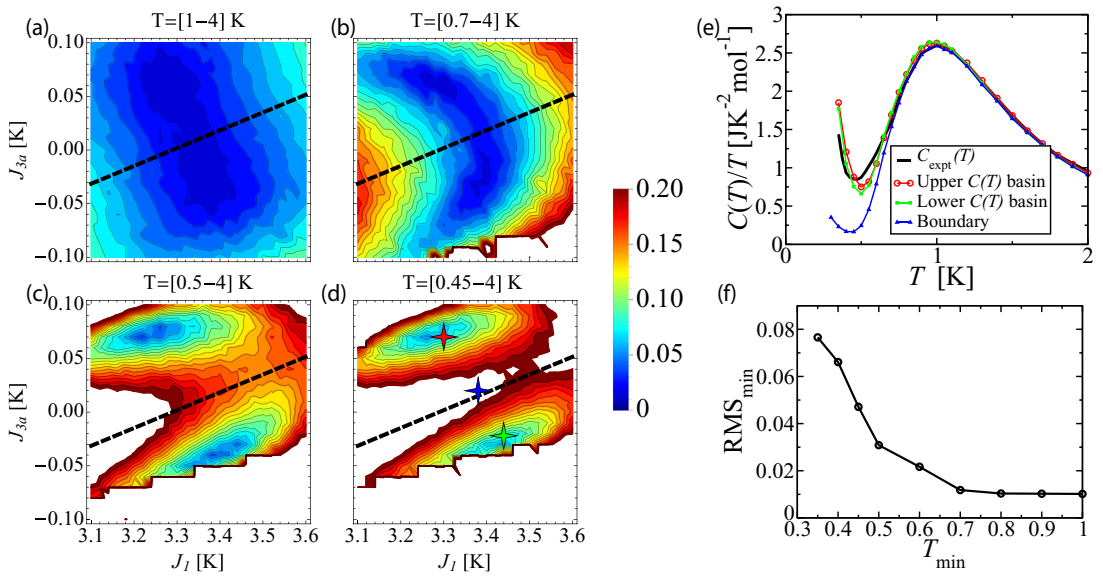

FIG. 5. Goodness of fit of Monte Carlo data compared to experimental specific heat. (a)–(d) RMS error deviation σ_C of the dipolar spin ice model in a constrained J_1-J_{3a} parameter space compared to recently reported specific-heat measurements [30]. The experimental specific-heat data displayed in (e) are the raw data minus the calculated nuclear portion $C_{\rm expt}(T) \equiv C_{\rm raw}(T) - C_{\rm nuc}(T)$ (see Appendix D). The label above each panel gives the temperature range of the fit. A dark blue color indicates a good fit, while white regions are off the scale. (e) Specific heat divided by temperature for the experimental data (thick black line), a representative point in the upper basin (red open circles and red line), a representative point in the lower basin (filled green up triangles and green line) and a point on the boundary (filled blue squares and blue line). The corresponding J_1-J_{3a} points are marked by correspondingly colored stars in (d). (f) The minimal RMS error in the entire J_1-J_{3a} plane as a function of the lower limit of the temperature range of the fit $T_{\rm min}$. Note the rapid increase in the RMS error below $T \approx 0.7$ K, indicating the rapid onset in the failure of the model to describe the experimental specific-heat data $C_{\rm expt}(T)$.

and thus significantly smaller than the $\sim$9.9 $\mu_{\rm B}$ value in $Dy_2Ti_2O_7$. In practice, this means that the net hyperfine contact interaction $A\langle J^z\rangle$, arising in the nuclear hyperfine term $A\boldsymbol{I}\cdot\boldsymbol{J}$, where $\boldsymbol{I}$ is the nuclear spin and $\boldsymbol{J}$ is the total electronic spin, was implicitly taken to be roughly $9.9/4.5 \sim 2.2$ times too small in Ref. [30]. Since Dy^{3+} has very strong Ising easy-axis anisotropy in $Dy_2Ti_2O_7$, the nuclear partition function fully factorizes out from the electronic one [62]. As the nuclear specific heat scales as $\sim A^2\langle J^z\rangle^2/T^2$ for temperature $T \gg A\langle J^z\rangle$, we argue that the nuclear specific heat estimated at $T \sim 0.5$ K in Ref. [30] to be about 4.5 times too small. Appendix D discusses in more detail the subtraction of the nuclear specific heat $C_{\rm nuc}(T)$ from the raw experimental data $C_{\rm raw}(T)$, reported in Ref. [30], with the magnitude of the correction displayed in Fig. 18. In what follows, we refer to the experimental (electronic) magnetic specific heat $C_{\rm expt}(T)$ to be compared with the Monte Carlo data, defined as $C_{\rm expt}(T) \equiv C_{\rm raw}(T) - C_{\rm nuc}(T)$.

2. *Magnetic specific heat*

Similarly to the analysis of the neutron scattering data, a goodness of fit parameter is required to assess the ability of the model to describe the experimental specific-heat data $C_{\rm expt}(T)$ against the Monte Carlo simulation data $C_{\rm MC}(T)$. In this study, we calculate the specific-heat goodness of fit σ_C according to

$$\sigma_C^2 = \sum_{i=1}^{N_T} \frac{[C_{\rm MC}(T_i) - C_{\rm expt}(T_i)]^2}{T_i^2 N_T}, \qquad (8)$$

and we use $N_T = 42$ distinct temperatures T_i between $T = 0.45$ and 4 K. The experimental data $C_{\rm expt}(T_i)/T_i$ come from three different sources: below $T = 0.8$ K from Pomaranski *et al.* [30], between 0.8 and 1.4 K from Klemke *et al.* [33], and above 1.4 K from Higashinaka *et al.* [34]. By applying a cubic spline fit to the experimental data, suitable temperature points T_i were selected.

We display in Fig. 5 the RMS deviation σ_C of Monte Carlo data $C_{\rm MC}(T)$ from $C_{\rm expt}(T)$ (see Sec. II B), which we refer to as RMS in Figs. 5(a)–5(d) and Fig. 5(f). The temperature interval for the comparison is extended from [1–4] K in Fig. 5(a) to [0.45–4] K in Fig. 5(d). We find a single wide basin of low $\sigma_C \sim 0.01$ for the [1–4] K high-temperature range [Fig. 5(a)], but observe that the quality of the fit deteriorates rapidly to $\sigma_C \sim 0.08$ with two separate basins of lowest σ_C developing when the temperature range is extended to include the experimental upturn at $T \lesssim 0.5$ K [Fig. 5(d)].

If the upturn in the experimental specific heat were caused by an impending ordering transition in the material at a critical temperature $T_c \sim$ [0.25–0.30] K, we would expect that points away from the phase boundary would naturally yield a better fit to the experimental data since the transition temperature is suppressed by phase competition in the vicinity of the boundary, as was explicitly demonstrated in Fig 3. To further analyze this, we display in Fig. 5(e) the specific heat for a point in the upper basin ($J_1 = 3.30$, $J_{3a} = 0.07$), the lower basin ($J_1 = 3.44$, $J_{3a} = -0.02$), and on the boundary ($J_1 = 3.38$, J_{3a}=0.02). As expected, the specific heat at the two points away from the boundary turn up at a higher temperature and therefore yield a somewhat better match to the experimental

data. However, note that as the temperature range of the fit is extended below $T_{\min} = 0.7$ K there is really *no* point in the parameter space that matches the experimental data well. In Fig. 5(f), we plot the minimal RMS error ($\mathrm{RMS}_{\min}$) in the entire J_1-J_{3a} plane as a function of the lower limit of the temperature range of the fit $T_{\min}$.

The rapid increase of the RMS error below 0.7 K indicates that the observed rise of the specific heat is not caused by an impending ordering transition in the material since the model of Eq. (1) should naively be able to describe such a transition while maintaining a not too strongly temperature-dependent RMS deviation between $C_{\mathrm{MC}}(T)/T$ and $C_{\mathrm{expt}}(T)/T$. The reason for this increase in the RMS deviation is that the ordering transition for parameter points far away from the boundary is strongly first order, as was shown in Fig 3. We would therefore expect only small pretransitional fluctuations, and a very rapid and sudden rise of the specific heat. The Monte Carlo results for the two basins (red and green curves) fall deeper than the experimental (black) curve, and rise more rapidly, indicating that the experimental data are unable to keep up with the first-order transition of the DSM with J_{ij} parameters corresponding to the upper or lower basin. In the next section, we further elaborate on this point by making a detailed comparison of the neutron scattering and specific-heat data (see in particular Fig. 9).

E. Comparison of neutron data and specific heat

In the previous two sections we found that the neutron scattering structure factor $S(\boldsymbol{q})$ indicates an exchange parameter set close to the phase boundary between the two relevant ordered phases, while the recent specific-heat data are more compatible with a parameter set well within one of the two ordered phases. To examine which alternative is most likely, we begin by ruling out the existence of a region in the parameter space that reconciles the $S(\boldsymbol{q})$ and $C_{\mathrm{expt}}(T)$ measurements. We choose to characterize $S(\boldsymbol{q})$ by the ratio $r \equiv S(0\ 0\ 3)/S(\frac{3}{2}\ \frac{3}{2}\ \frac{3}{2})$, which we found in Sec. III C to be a revealing overall indicator of the spin-spin correlations in $Dy_2Ti_2O_7$. For the specific heat we consider the $C_{\mathrm{expt}}(T)/T$ RMS deviation σ_C. We divide the J_1-J_{3a} space into a grid of points for which we calculate the ratio r and σ_C. We choose to calculate the neutron scattering ratio r at $T = 1.3$ K since we know that there are no experimental equilibration issues at this temperature. The specific-heat deviation σ_C was evaluated for the [0.45–4] K temperature interval in order to include the experimentally observed upturn in the specific heat. In Fig. 6, we plot r versus σ_C for all the points in the J_1-J_{3a} space. In order to accommodate both experiments, the r coordinate for a point should be close to the experimental value $r \cong 1.13$ at $T = 1.3$, while σ_C should be small. In Fig. 6, we have indicated the experimental value of $r = 1.13$ with a red band, and a good specific heat match ($\sigma_C < 0.2$) with a blue band. We note that there are points within the red band: these correspond to parameter values in the boundary region. We also note that there are *no* points within the blue band, emphasizing the conclusion of the previous section that there is *no* parameter set able to match the recent specific-heat data well, irrespective of the quality of fit to the neutron scattering data. The two branches of the scattered points that reach a minimum σ_C of about 0.04 correspond to points in the upper and lower basins, discussed in the previous section. Hence, the present model is unable to *simultaneously* describe the specific heat [$C_{\mathrm{expt}}(T)$] and neutron scattering [$S(\boldsymbol{q})$] experiments. We have performed extensive Monte Carlo simulations to verify that this conclusion still holds if we add a nonzero fourth-nearest-neighbor interaction J_4 and relax the [112] experiment-based constraints well beyond the optimal Eqs. (4) and (5), as detailed in Appendix A. For Fig. 6 we have considered parameters in the range (all in units of Kelvin) $2.8 < J_1 < 4.0$, $|J_{3a}| < 0.15$, and $|J_4| < 0.15$, with corresponding J_2 and J_{3b} values given by Eqs. (5) and (4), respectively. Note that the conclusion of this analysis also holds if we calculate the neutron ratio r at $T = 0.3$ K and compare our Monte Carlo result to the experimental value at this lower temperature.

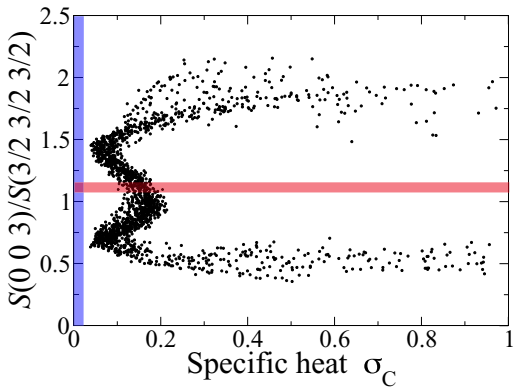

FIG. 6. Ratio of neutron intensity versus goodness of specific-heat fit in Monte Carlo. The J_1-J_{3a} space has been parametrized on a mesh. For each point, the structure factor ratio $r \equiv S(0\,0\,3)/S(\frac{3}{2}\ \frac{3}{2}\ \frac{3}{2})$ at $T = 1.3$ K is displayed against the specific-heat deviation from experiment [30], σ_C for the [0.45–4] K temperature interval. The horizontal red band is centered at the experimental ratio of $r \cong 1.13$, while the vertical blue band indicates the region of a good match with the experimental data ($\sigma_C < 0.2$). Note that there are no points close to the intersection of the two bands. Such points would represent parameter sets that model *both* the experimental neutron scattering and specific-heat data well.

To further assess the likelihood of a parameter set in the upper or lower basin versus a parameter set on the boundary, we explicitly calculate $S(\boldsymbol{q})$ for the three parameter points indicated by stars in Fig. 5(d). In addition, we show results for the parameter set determined in Ref. [36], referring to this particular parameter set as the "g-DSM*." A summary of the naming convention and parameter values we examine are given in Table I. In Figs. 7(a)–7(d) we display the neutron

TABLE I. Named parameter sets. The first three sets are indicated by stars in Fig. 5(d). In all cases, the dipolar constant $D = 1.3224$ K and all parameter values are given in Kelvin.

Model	J_1	J_2	J_{3a}	J_{3b}
Upper	3.30	−0.0949	0.07	−0.0167
Boundary	3.38	−0.1349	0.02	0.0167
Lower	3.44	−0.1649	−0.02	0.0433
g-DSM*	3.41	−0.14	0.025	0.025

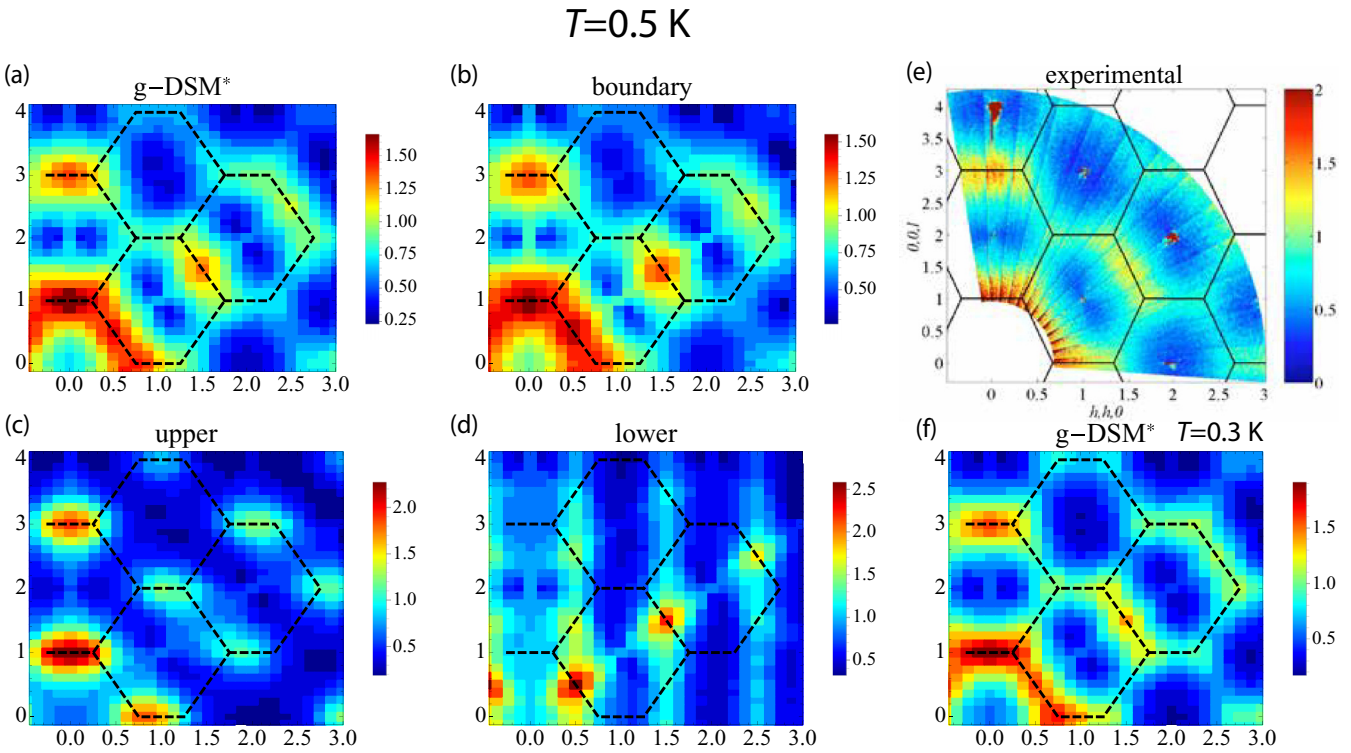

FIG. 7. Monte Carlo simulation results for the neutron structure factor $S(\boldsymbol{q})$ at $T = 0.5$ K calculated for the four parameter sets in Table I in panels (a)–(d). The maps can be compared to the experimentally measured structure factor at $T = 0.3$ K in panel (e) (Ref. [40]). Points of interest are the broad intensity maxima centered around $\boldsymbol{q} = (0\,0\,3)$ and $\boldsymbol{q} = (\frac{3}{2}\ \frac{3}{2}\ \frac{3}{2})$ and the ZBS pattern. Note that the experimental intensity maximum at $\boldsymbol{q} = (\frac{3}{2}\ \frac{3}{2}\ \frac{3}{2})$ is more closely matched by the structure factor for the g-DSM* parameter set calculated at $T = 0.3$ K, shown in panel (f).

scattering structure factor for these four parameter sets. The results can be compared to the experimental structure factor, nominally measured at $T = 0.3$ K. The experimental data agree remarkably well with the structure factor calculated for the point on the boundary and the g-DSM* parameter set, while there are major differences between the experimental data and the results for the parameter values in the upper and lower basins. Also note that the Monte Carlo result for the g-DSM* parameter set at $T = 0.3$ K, shown in Fig. 7(f) appears even closer to the experimental result than Fig. 7(a). This is surprising since, as argued in Sec. III C, one could expect the sample to freeze around $T = 0.5$ K. We therefore take Fig. 7 as further strong evidence that the appropriate parameter set for $Dy_2Ti_2O_7$ is located close to the phase boundary. We arrive at the very same conclusion by considering Fig. 8, which makes the same comparison as Fig. 7, but at the elevated temperature $T = 1.3$ K, where the sample is well equilibrated.

We conclude this section by examining the low-temperature behavior of the specific heat and entropy of the four parameter points examined in the previous paragraph. Using the Monte Carlo method, we calculate $C(T)/T$ and integrate this function to obtain the entropy $S(T)$. The result is shown in Fig. 9. Consider first the upper panel showing the specific heat. The specific heat for the points in the upper and lower basins rises very abruptly due to the strong first-order transition and lack of pretransitional fluctuations, as discussed in the previous subsection. The transition temperature is in the 0.30–0.32 K interval, immediately below the last experimentally measured temperature of 0.34 K in Ref. [30]. This suggests that if specific-heat measurements could be carried out to slightly lower temperature than the one considered in Ref. [30], one could experimentally resolve whether the upturn is indeed caused by an ordering transition as described by the g-DSM. In the lower panel of Fig. 9, we find that the Pauling plateau is not developed over any significant temperature interval for the parameter points in the upper and lower basins, while it is clearly visible in the 0.2–0.6 K range for the points close to the boundary (including the g-DSM*).

While we find that there is no parameter set that is compatible with both neutron scattering data and the recent specific-heat measurements down to 0.34 K, we do find that neutron scattering data down to nominally 0.3 K and specific-heat data *above* 0.7 K are *both* consistent with a parameter set placing $Dy_2Ti_2O_7$ near the boundary between two competing long-range-ordered ice-rule obeying states. While the low-temperature rise in the specific heat could indicate a parameter set in the upper or lower basin, we find this unlikely since our analysis shows that these parameter points yield spin-spin correlations that are incompatible with neutron scattering data already at 1.3 K.

While it was not obvious before initiating this study, we have discovered that the g-DSM* parameter set of Ref. [36] almost satisfies our J_1-J_2 and J_{3a}-J_{3b} constraints, and is also located very close to the phase boundary. It therefore appears that the $J_{3a} = J_{3b}$ constraint assumed in Ref. [36] is almost realized in $Dy_2Ti_2O_7$, although this was not *a priori* evident.

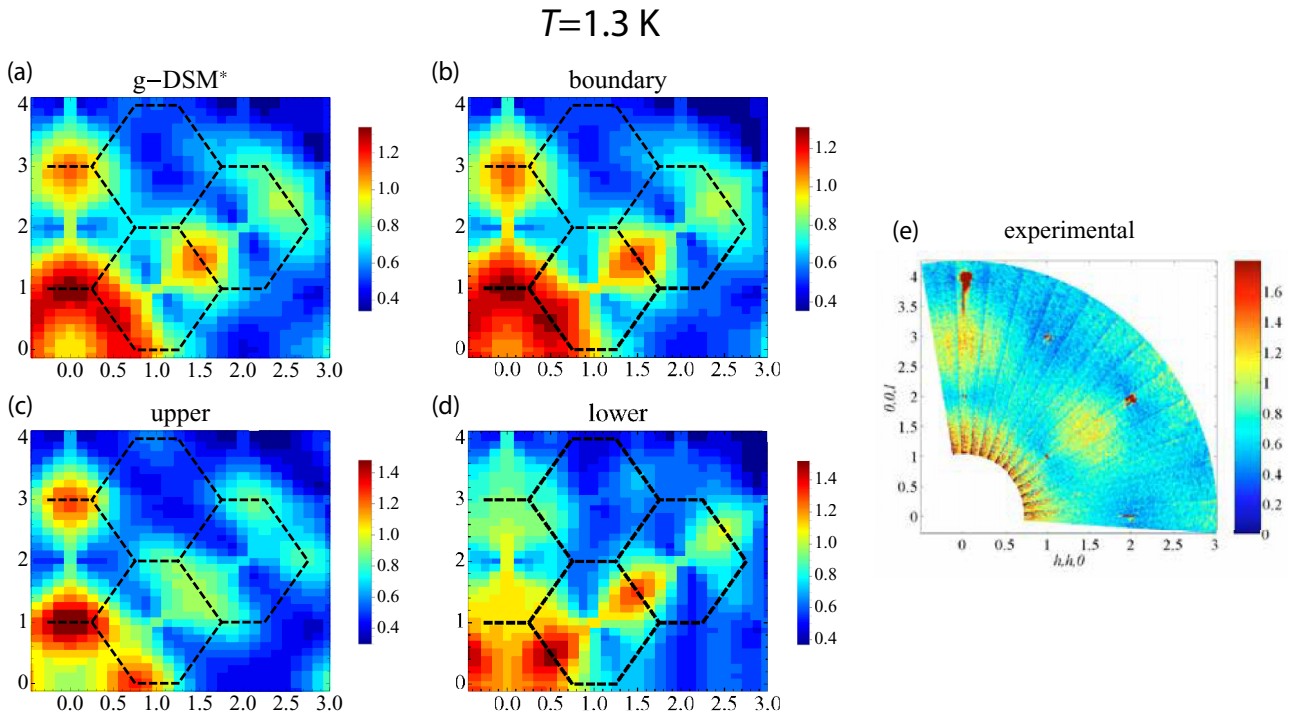

FIG. 8. Monte Carlo simulation result for the neutron structure factor $S(\boldsymbol{q})$ at $T = 1.3$ K calculated for the four parameter sets in Table I. The maps can be compared to the experimentally measured structure factor at $T = 1.3$ K in panel (e) (Ref. [40]). Points of interest are the broad intensity maxima centered around $\boldsymbol{q} = (0\,0\,3)$ and $(\frac{3}{2}\ \frac{3}{2}\ \frac{3}{2})$ and the remnants of the ZBS pattern, more clearly seen in Fig. 4(a).

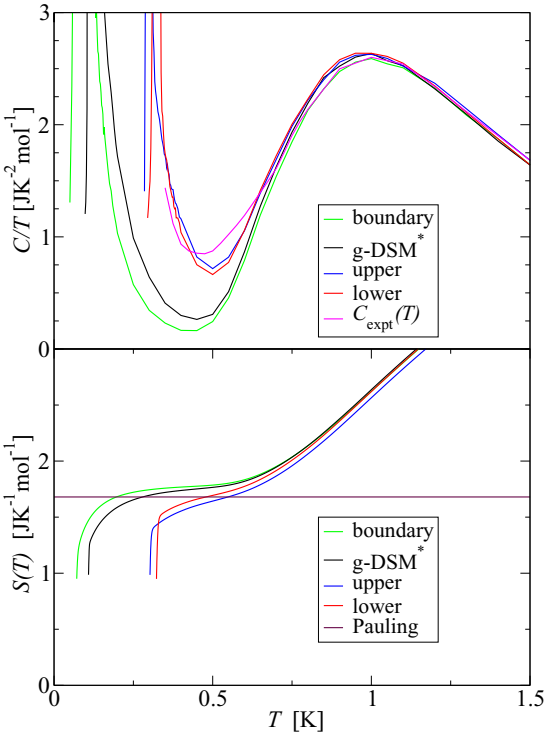

FIG. 9. The specific heat (upper panel) and corresponding entropy $S(T)$ (lower panel) for the four parameter sets in Table I. The entropy value of the Pauling plateau at $S = (R/2)\ln(\frac{3}{2})$ is indicated by a brown horizontal line in the lower panel.

One should note that the main goal of Ref. [36] was to investigate to what extent a model of finite-size clusters of magnetic moments can describe the neutron scattering in the spin ice regime of $Dy_2Ti_2O_7$. It was not aimed at determining an optimal exchange parameter set for this compound. That notwithstanding, the present analysis confirms that the g-DSM* parameter set of Ref. [36] appears fairly appropriate for $Dy_2Ti_2O_7$. For example, one notes that the g-DSM* parameter set has also been found to accurately model a [111] field experiment [36], as well as the specific heat for a number of diamagnetically diluted samples of $Dy_{2-x}Y_xTi_2O_7$ [63] for temperatures above $T \sim 0.5$ K.

To summarize: The fact that the parametrization of the g-DSM obtained on the basis of the main generic neutron scattering features does not match the recent carefully equilibrated specific-heat measurements [30] in the *lower* temperature range 0.35–0.7 K leads to *the second main result* of our study: the upturn in the specific heat is a strong indication that, at temperatures below 0.7 K, some new physics becomes relevant which cannot be readily exposed by the model of Eq. (1). Exploring two such possible causes is the topic of the next subsection.

F. Quantum effects and random disorder

From our analysis of the neutron scattering data, we conclude that the recently observed upturn in the specific heat is not caused by an impending ordering transition within the g-DSM. We therefore consider what would seem the next most likely causes of the specific-heat upturn below $T \sim 0.5$ K: quantum effects and random disorder.

1. *Quantum effects and non-Ising exchange*

An intriguing possibility is that quantum effects could be responsible for the increasing specific heat below 0.5 K as found at low temperatures in simulations of a spin-$\frac{1}{2}$ XXZ model on the pyrochlore lattice [45]. In this context, Ref. [41] considers the effects of a hexagonal "ring exchange" tunneling term on the g-DSM, and finds that if the tunneling amplitude g is greater than the classical ordering temperature T_c for $g = 0$, a quantum spin liquid state may be stabilized. Given our conclusion that $Dy_2Ti_2O_7$ is located at the phase boundary between two classical ordered states, where the critical temperature is suppressed to about $T_c \sim 70$ mK (see Fig. 3), it is perhaps conceivable that quantum (non-Ising) terms become relevant at higher temperatures than previously thought. We note that a simple spin-$\frac{1}{2}$ XXZ model results in a tunneling strength $g = 12\frac{J_\pm^3}{(J_{zz})^2}$, where J_{zz} and $J_\pm$ are the longitudinal (Ising) and transverse (XY) exchange couplings [64]. The Monte Carlo work of Ref. [45] finds that the specific heat in such a model starts to increase below a crossover temperature $T^* \sim g$. To assess whether g is large enough in $Dy_2Ti_2O_7$ to cause the upturn in the specific heat at a temperature $T^* \sim 0.5$ K, we analyze the expected scale of the quantum corrections to the Ising part of the Hamiltonian (1).

One possible route to transverse couplings comes from quantum corrections to the effective Hamiltonian through virtual crystal-field excitations [65]. Due to the large gap $\Delta \sim 300$ K to the first-excited crystal-field level and the $J_{\rm eff} \equiv [5D - J_1]/3 \sim 1$ K scale of the interactions acting within the full crystal-field manifold, quantum corrections can be expected to appear perturbatively at a temperature of order $J_\pm \sim J_{\rm eff}^2/\Delta \sim 3$ mK and are therefore not detectable at a temperature of 0.5 K. Off-diagonal terms can also appear through the interaction of high-rank multipoles [46,47] involving the $\boldsymbol{J} = \frac{15}{2}$ angular momentum components within the ${}^6H_{15/2}$ ground-state electronic manifold of Dy^{3+}. Due to the dominant $|\pm\frac{15}{2}\rangle$ composition of the ground-state crystal-field doublet [15,16], the largest contributions to the transverse $S^\pm$ effective spin-$\frac{1}{2}$ operators would originate from rank-15 multipolar interactions between the Dy^{3+} ions [47]. The most significant source of such multipolar interactions are superexchange processes mediated through the neighboring oxygen ions [47]. However, these superexchange processes predominantly generate interactions between multipoles of rank seven or less [46,47,66]. Such multipole interactions will thus only connect the subleading spectral components of the crystal-field ground-state doublet $C_{m_J}|J = \frac{15}{2}, m_J\rangle$, $m_J \neq \pm\frac{15}{2}$. From the experimentally observed large magnetic moment $\mu \sim 10\ \mu_{\rm B}$ of Dy^{3+} in $Dy_2Ti_2O_7$, we can infer that these small C_{m_J} components are at most $C_{m_J} \sim 10\%$ of the leading $C_{m_J=\pm 15/2} \approx 1$ component [47].

With $J_{zz} \sim 4J_{\rm eff}$ and $J_\perp \sim 4(C_{m_J})^2 J_{\rm eff}/(C_{15/2})^2$, where the prefactor 4 arises from moving from the Ising $S_i^z = \pm 1$ convention in this work to the $S = \frac{1}{2}$ convention of Ref. [64], we therefore expect g to be at the scale $g \sim 0.05$ mK. Thus, despite the much suppressed critical temperature $T_c \sim 70$ mK that we exposed above (see Fig. 3), we argue that quantum effects are unlikely to be responsible for the rise in the specific heat detected at a temperature $T^* \sim 0.5$ K given that $T_c/g \sim 10^4$, hence far up in the classical dipolar spin ice regime, unlike in the proposal of Ref. [41]. While we expect that further calculations would lead to a more accurate estimation of $J_\perp$, and thus of g, it would seem unlikely to lead to a rescaling of g by four orders of magnitude.

After having argued that the rise of $C_{\rm expt(}T)$ below $T^* \sim 0.5$ K cannot be explained by a classical dipolar spin ice model that consistently describes the neutron scattering data, we have now argued that the same rise cannot originate from the development of a quantum coherent regime below T^*.

2. *Random disorder*

Another potential origin for the rise of the electronic specific heat at $T \lesssim 0.5$ K is a Schottky-type response induced by random disorder. It was recently demonstrated that disorder, in the form of local magnetic impurities, may explain the long-time relaxation in $Dy_2Ti_2O_7$ (Ref. [29]). Possible physical realizations of disorder include stuffed spins [42,43] or local Dy^{3+} moments with easy-plane anisotropy due to oxygen vacancies affecting the crystal field [31] or the concomitant magnetic Ti^{3+} magnetic impurities. We now illustrate that such a generic phenomenon could explain the rise of $C(T)$ for $T \lesssim 0.5$ K.

The quantitative microscopic description of the effects of disorder in highly frustrated magnetic materials is a complex and rich problem [13,14]. In the present case, the complexity of such a task is further compounded by the fact that all pertinent forms of random disorder (e.g., oxygen vacancies, stuffing, etc.) have not yet been fully identified and their effects quantified in $Dy_2Ti_2O_7$. It appears that the problem of dilution of the magnetic Dy^{3+} and Ho^{3+} ions by nonmagnetic Y^{3+} in $Dy_2Ti_2O_7$ and $Ho_2Ti_2O_7$ is the simplest case of random disorder, with a description in terms of a mere site-diluted version of a dipolar spin ice model accounting well for the specific-heat data for $T \gtrsim 0.5$ K in $Dy_{1-x}Y_xTi_2O_7$ and $Ho_{1-x}Y_xTi_2O_7$ [63] (see, however, the recent work in Ref. [67]). On the other hand, we expect the microscopic description of oxygen vacancies or rare-earth ions stuffing the pyrochlore B site normally occupied by nonmagnetic transition-metal ions, and its ultimate quantitative description via a controlled numerical calculation, to be significantly more complicated. Indeed, one would expect that deformation of the superexchange pathways and modifications of the local crystal field would occur. This would result in a randomization of the J_{ij} exchange couplings and of the dipolar coupling ($D \to D_{ij}$) as well as possibly induce non-Ising (transverse) exchange terms coupling the other components of the effective spin-$\frac{1}{2}$ describing the crystal-field doublet of Dy^{3+}. In this work, we consider a minimal model of dilute random disorder in $Dy_2Ti_2O_7$. Our goal is not to develop a quantitative description of the role of disorder on the low-temperature properties of $Dy_2Ti_2O_7$. Rather, we wish to illustrate that the *generic* effects of dilute random disorder with a realistic energy scale Ω could perhaps naturally explain the rise of $C_{\rm expt}(T)$ for $T \lesssim T^*$.

With this agenda spelled out, we now proceed and consider the effects of stuffed spins in the model defined by Eq. (1) for $Dy_2Ti_2O_7$. The stuffed spins are coupled to the Dy^{3+} pyrochlore backbone through Eq. (3), the Ω model. We perform loop Monte Carlo simulations for varying stuffing percentages

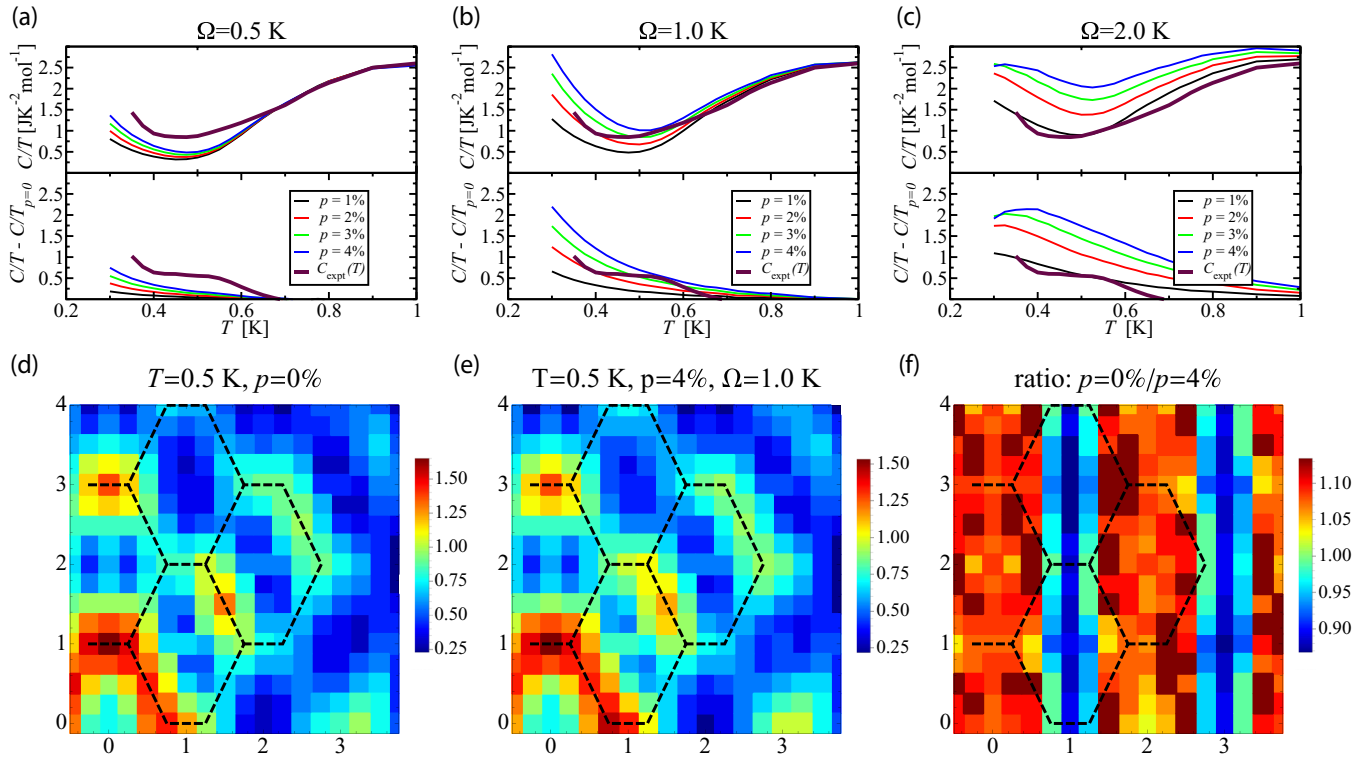

FIG. 10. Effects of impurities on specific heat and neutron scattering. Specific heat $C(T)/T$ for the Ω model with (a) $\Omega = 0.5$ K, (b) $\Omega = 1.0$ K, and (c) $\Omega = 2.0$ K with the percentage of stuffed spins $p = 1\%, 2\%, 3\%$, and 4%. The upper panel shows the total specific heat, while in the lower panel the specific heat of the clean system ($p = 0$) has been subtracted from the disorder average of the upper panel revealing the impurity contribution. The neutron structure factor $S(\boldsymbol{q})$ for the disorder-free ($p = 0$) g-DSM model [36] at $T = 0.5$ K is shown in (d) and with $p = 4\%$ stuffed spins included in (e). The last panel (f) shows the ratio of the structure factor for the clean (d) and stuffed (e) systems.

p and coupling constants Ω and display the results in Fig. 10. Disorder averages have been performed over 32 independent disorder configurations since the variation between different configurations is quite small. Figures 10(a)–10(c) contain the specific-heat data for $\Omega = 0.5$, 1.0, and 2.0 K, respectively. Results for stuffing percentage $p = 1\%$, 2%, 3%, and 4% along with the experimental result are shown in the upper subpanels, while in the lower subpanels we have subtracted the specific heat for the clean g-DSM model, exposing the impurity contribution to the specific heat. We see that, at least for $\Omega = 0.5$ and 1.0 K, the impurity contribution is roughly linear in p, indicating predominantly independent impurities. The impurity contribution also shifts to higher temperature as Ω is increased, as we would expect from a simple two-state Schottky model. In this case, the scaling is more complicated since each impurity spin interacts with the electronic spin on the six nearest neighbors, and we would expect the stuffed spin to effectively renormalize the local couplings. Again, our goal is not to perform an exhaustive study of this specific model. Rather, we wish to illustrate that such a simple effective local impurity model can cause an upturn in rough qualitative agreement with the measured specific heat with a stuffing ratio at the 1% level and a realistic $\Omega = 1$ K energy scale. Interestingly, we also note that this level of stuffing does not produce a very strong response in the neutron structure factor. In Figs. 10(d) and 10(e), we display the calculated $S(\boldsymbol{q})$ for the g-DSM model with $p = 0\%$ and 4% stuffing, respectively. The disorder average has here been performed over 96 disorder configurations. The effects are rather hard to discern in an energy-integrated scattering profile (i.e., equal-time correlations computed through the present classical Monte Carlo simulations) with the ratio of the two scattering intensity profiles, plotted in Fig. 10(f), showing a change of about 10%. With the recent realization that stuffing of the heavy rare-earth (RE) ions (RE = Yb, Er, Ho) is at play in $Yb_2Ti_2O_7$, $Er_2Ti_2O_7$, and $Ho_2Ti_2O_7$ (i.e., RE^{3+} replacing Ti^{3+}) [42,43], it would appear plausible that some level of stuffing may also occur in $Dy_2Ti_2O_7$ given that the ionic radius of Dy^{3+} is only $\sim$1% larger than Ho^{3+} [68]. Further experimental investigations are required to assess whether or not this is the case. While 1% stuffing is possibly a bit too high for $Dy_2Ti_2O_7$ samples, our results do show that *effective* local random magnetic disorder in the g-DSM associated with an energy scale $\Omega \sim 1$ K can in principle capture the essential features observed in calorimetric measurements without creating a significant contradiction with available neutron scattering data.

IV. CONCLUSION

In summary, this study gives a natural interpretation of the main features of the structure factor $S(\boldsymbol{q})$ observed in neutron scattering measurements on the $Dy_2Ti_2O_7$ spin ice material in terms of competing phases. Remarkably, we find that neutron

scattering experiments on a single crystal of $Dy_2Ti_2O_7$ place the material at the most interesting point in the phase diagram, i.e., precisely near the boundary between competing single- and double-chain long-range-ordered phases. This region displays unusual properties including masked ground-state order and extremely slow magnetic relaxation associated with the coarsening of stacking defects. We expect the equilibration of these defects to be a further mechanism, beyond the mere dynamical arrest associated with the ice-rule formation, impinging on the approach to equilibrium of $Dy_2Ti_2O_7$.

The observation of such accidental competing ground states suggests that $Dy_2Ti_2O_7$ could be extremely sensitive to random disorder or quantum fluctuations. Furthermore, our analysis of the recently observed upturn in the specific heat [30] shows that this is caused by terms not present in the classical generalized dipolar spin ice model. Quantum corrections appear to be much too small in magnitude to become noticeable at temperatures as high as $T^* \sim 0.5$ K where recent thermally equilibrated specific-heat measurements [30] find an upturn, even after correcting for the nuclear specific heat. We therefore believe that random disorder, either in the form of low level of stuffing [43] or oxygen vacancies [31], or both, is the most likely source of the upturn. There is also an interesting scenario in which random disorder could, by lowering the local symmetry of the crystal field, destroy the local Ising nature of the moments and induce quantum fluctuations in the nearby Dy^{3+} moments. A study that would assess the level of Dy^{3+} stuffing onto the B site otherwise occupied by Ti^{4+} in $Dy_2Ti_2O_7$, as was done in Ref. [43] for $Ho_2Ti_2O_7$, $Er_2Ti_2O_7$, and $Yb_2Ti_2O_7$, would therefore be highly desirable. More well-equilibrated experimental studies of a variety of samples will be required to determine the exact nature of such impurities and their specific role on the low-temperature thermodynamic properties of $Dy_2Ti_2O_7$. As a corollary, our work suggests that a (fairly) well-defined Pauling plateau may be observed in well-equilibrated measurements on samples of high-stoichiometric purity. Perhaps the most important conclusion of our work is the following one: Notwithstanding the fact that the two disorder-free models that are partially able to describe the specific-heat data between 0.35 and 0.7 K are inconsistent with the main neutron scattering features, both models predict a phase transition to long-range order near 0.30 K. Consequently, it would seem imperative to push the low-temperature limit of well-equilibrated calorimetric measurements down to, say, 250 mK. This work predicts that the disagreement with the best classical dipolar spin ice model for $Dy_2Ti_2O_7$ would then become vividly manifest, with such an experiment providing important clues as to the ultimate low-temperature fate of the spin ice state in this archetypal spin ice material.

ACKNOWLEDGMENTS

It is a pleasure to thank our experimental colleagues D. Pomaranski and J. Kycia (specific heat), Sakakibara and Hiroi ([112] experiment), and T. Fennell (neutron scattering) for sharing their data and for stimulating discussions. We also acknowledge N. Shannon and P. McClarty for useful discussions. This work was supported in part by the NSERC of Canada and the Canada Research Chair program (M.G., Tier 1). P.H. is grateful for the computer support of PDC-HPC (Ferlin) at KTH and the financial support by the Stenbäck Foundation and the Swedish Research Council. J.A. acknowledges support from the NSERC of Canada. F.F. acknowledges support from a Lindemann Trust Fellowship of the English Speaking Union. The numerical work at the University of Waterloo was made possible by the facilities of the Shared Hierarchical Academic Research Computing Network (SHARCNET:www.sharcnet.ca) and Calcul Canada. M.G. acknowledges support from the Canada Council for the Arts and the Perimeter Institute (PI) for Theoretical Physics. Research at PI is supported by the Government of Canada through Industry Canada and by the Province of Ontario through the Ministry of Economic Development & Innovation.

APPENDIX A: PARAMAGNETIC CONSTRAINTS FROM [112] MAGNETIZATION MEASUREMENTS

The constraints that we invoke between the J_{ij} couplings to analyze the specific-heat and neutron data in the main part of the paper result from considerations of an experiment in which a strong magnetic field is applied near the cubic [112] direction [37–39]. The main effect of the field is to maximally polarize the moments along their local [111] Ising directions on three of the four fcc sublattices that comprise the pyrochlore lattice and which form *kagome* layers. The spins on the remaining sublattice form *triangular* layers [2], as illustrated in Fig. 2. Spins on these triangular layers interact with each other only through the dipolar and third-nearest-neighbor interactions J_{3a} and J_{3b} since they reside on the same fcc sublattice [69]. While the spins on the "triangular sites" are perpendicular to, and thus decoupled from, the [112] field component, they are still subject to an internal field $h_{\rm int}$ from the polarized spins on the kagome layers. This internal field enforces the ice rules so that the spins in the triangular layers point "in" along the $[\bar{1}\bar{1}1]$ direction (see Fig. 2). Experimentally, this internal "ice-rule" enforcing field can be canceled by rotating the applied external field away from the [112] direction [37,39,70], so that it acquires a component $h^{[\bar{1}\bar{1}1]}$ in the $[\bar{1}\bar{1}1]$ direction parallel to the Ising axis of the "triangular spins" (see Fig. 2). By tuning this $[\bar{1}\bar{1}1]$ field component, one eventually reaches a critical field value $h_{\rm c}^{[\bar{1}\bar{1}1]}$ when the $[\bar{1}\bar{1}1]$ field component cancels out the ice-rule enforcing field $h_{\rm int}$. The experimentally measured value of the cancellation field is $h_{\rm c}^{[\bar{1}\bar{1}1]} \equiv -h_{\rm int} = -0.28 \pm 0.02$ T (the negative sign arises because the applied field has to oppose the ice-rule enforcing field $h_{\rm int}$ which is along $[\bar{1}\bar{1}1]$) [38,39]. Theoretically, the cancellation field can be expressed in terms of our model Hamiltonian (1) of the main text, as

$$h_{\rm c}^{[\bar{1}\bar{1}1]}({\rm T})\mu_{\rm Dy}k_{\rm B} = \tfrac{2}{3}J_1 + \tfrac{4}{3}J_2 - 2.972D, \qquad \text{(A1)}$$

keeping exchange couplings J_{ij} up to third-nearest-neighbor exchange interactions. Since J_{3a} and J_{3b} connect spins on the same sublattice they do not contribute to the internal field $h_{\rm int}$. The dipolar contribution $-2.972D$ was computed using the Ewald summation method [23]. Using the above equation we obtain Eq. (4) of the main text:

$$J_2 = -\tfrac{1}{2}J_1 + \tfrac{3}{4}h_1, \qquad \text{(A2)}$$

where $h_1 = \mu_{\rm Dy} k_{\rm B} h_{\rm c}^{[\bar{1}\bar{1}1]}({\rm T}) + 2.972D$. Inserting $h_{\rm c}^{[\bar{1}\bar{1}1]} = -0.28 \pm 0.02$ T (Ref. [39]), $\mu_{\rm Dy} = 9.87\mu_{\rm B}$, and $D = 1.322$ (Ref. [36]) we find that $h_1 = 2.07 \pm 0.13$ K. In Fig. 6, the full range of h_1 within the experimental uncertainty was allowed, while for the other figures the optimal value of $h_1 = 2.07$ K was used.

A second constraint can be obtained for the third-nearest-neighbor interactions J_{3a} and J_{3b} by considering the susceptibility of the spins on the triangular layers. Again, experimentally, the field component in the $[\bar{1}\bar{1}1]$ direction can either be varied by a rotation of the applied field or by varying the vertical $[\bar{1}\bar{1}1]$ field. The susceptibility of the spins on the triangular planes (which form an fcc lattice) can therefore be measured as a function of that tunable $[\bar{1}\bar{1}1]$ field component. The susceptibility depends only on J_{3a}, J_{3b}, and D in our model Hamiltonian. Through this manipulation [37–39] of the applied magnetic field, it is thus possible to directly probe the effect of the third-nearest-neighbor exchange parameters on the thermodynamic properties of $Dy_2Ti_2O_7$ in a strong magnetic field near the [112] direction. We also note that, at the decoupling field $h_{\rm c}^{[\bar{1}\bar{1}1]}$, the above experiment results in an Ising face-centered-cubic magnet, which is normally not possible since a unique global easy-axis direction cannot be defined for a system with cubic global symmetry.

In the experiment of Ref. [39], the susceptibility as a function of the $[\bar{1}\bar{1}1]$ field component was measured at four different temperatures: $T = 0.29$, 0.41, 0.70, and 1.08 K. With the field component in the $[\bar{1}\bar{1}1]$ direction set precisely to the cancellation field value $h_{\rm c}^{[\bar{1}\bar{1}1]}$, the magnetic moments on the triangular layer undergo a transition to long-range ferromagnetic order at $T_{\rm c} \cong 0.26$ K (Refs. [37,38]). As a result, the $[\bar{1}\bar{1}1]$ susceptibility associated with this transition is divergent at $T_{\rm c}$ when the $[\bar{1}\bar{1}1]$ field $h^{[\bar{1}\bar{1}1]}$ is at its canceling value $h_{\rm c}^{[\bar{1}\bar{1}1]}$. When fitting the experimental susceptibility to our simulation data, the system needs to be sufficiently far away from the critical temperature to avoid strong finite-size effects in the simulations. However, the higher the temperature, the less "structure" the susceptibility has due to the decreasing correlation length, with the fit consequently becoming less constrained. Based on these two concerns, we select the data of Ref. [39] measured at 0.70 K.

We calculate the $[\bar{1}\bar{1}1]$ susceptibility in Monte Carlo simulations using a system size $L = 4$, and evaluate the goodness of fit according to

$$\sigma_\chi^2 = \frac{1}{N_h} \sum_{i=1}^{N_h} \left[\chi_{\rm MC}\left(h_i^{[\bar{1}\bar{1}1]}\right) - \chi_{\rm expt}\left(h_i^{[\bar{1}\bar{1}1]}\right)\right]^2, \qquad \text{(A3)}$$

where $\chi_{\rm MC}(h_i^{[\bar{1}\bar{1}1]})$ and $\chi_{\rm expt}(h_i^{[\bar{1}\bar{1}1]})$ are the Monte Carlo and experimental susceptibilities, respectively, determined at the applied $[\bar{1}\bar{1}1]$ field component $h_i^{[\bar{1}\bar{1}1]}$. The RMS deviation σ_χ is calculated for a total of $N_h = 38$ different values of $h_i^{[\bar{1}\bar{1}1]}$ ranging from -0.3184 to -0.2418 T. We display σ_χ in Fig. 11(a) as a function of J_{3a} and J_{3b}. In order to illustrate the nature and quality of the fit at a representative point, the experimental susceptibility $\chi_{\rm expt}$ is displayed along with $\chi_{\rm MC}$ calculated at $J_1 = 0.10$ K and $J_{3b} = -0.04$ K in Fig. 11(c). We also calculate and plot in Fig. 11(b) the difference between the maximum of the Monte Carlo and experimental susceptibilities

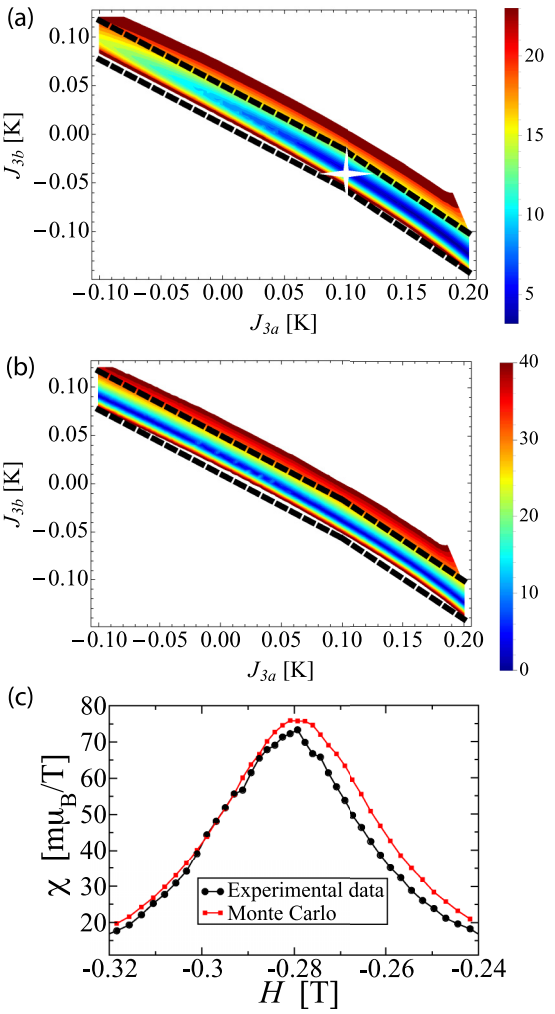

FIG. 11. Determination of the J_{3a}-J_{3b} constraining equation. Deviations of the susceptibility for the fcc sublattice (defined by the spins on triangular planes), calculated in the Monte Carlo simulations, from the experimental data [39] as a function of J_{3a} and J_{3b}. In (a), the RMS deviation σ_χ, calculated according to Eq. (A3), is shown, while in (b) the absolute value of the height difference, determined using Eq. (A4), is displayed. The dashed black lines show the parameter range used in Fig. 6 of the main text, while the optimal relationship lies precisely between the two lines. In (c), the susceptibility measured in the experiment and calculated in the Monte Carlo simulation at $J_{3a} = 0.10$ K and $J_{3b} = -0.04$ K [indicated by a white star in panel (a)] is shown on an absolute scale as a representative example.

precisely at the cancellation field

$$\Delta = \left|\chi_{\rm MC} - \chi_{\rm expt}\left(h_i^{[\bar{1}\bar{1}1]} = h_{\rm c}^{[\bar{1}\bar{1}1]}\right)\right|. \qquad \text{(A4)}$$

As we see in Figs. 11(a) and 11(b), the optimal fit falls on a slightly bent curve. The appearance of such a line can be understood within a mean-field interpretation. Since the susceptibility at a given temperature depends on the sum of the interactions, a decrease in the value of J_{3a} can be compensated for by an increase in the value of J_{3b}. This would keep the susceptibility constant and lead to a line with negative slope.

The optimal relations between J_{3a} and J_{3b} that result from this analysis are (all values in Kelvin)

$$J_{3b} = \begin{cases} -0.667 J_{3a} + 0.03 : & J_{3a} < 0.1, \\ -0.842 J_{3a} + 0.0474 : & J_{3a} > 0.1, \end{cases} \quad \text{(A5)}$$

which is Eq. (4). As a precaution, we also explored the parameter range beyond the above optimal equations and allowed J_{3b} to lie within ± 0.02 K of the optimal relation (quite a large range) as shown by the dashed lines in Figs. 11(a) and 11(b). This extended parameter space was used to generate Fig. 6 of the main text.

The constraint Eqs. (A2) and (A5) derived above apply to the case of a sufficiently large [112] magnetic field component such that, for the temperature $T = 0.7$ K considered to fit the data, one can safely ignore the thermal fluctuations of the spins on the kagome layers. For the temperatures relevant to this [112] experiment, this is readily achieved for a [112] field component larger than about 2 T [37–39]. One may then ask whether the constrained J_{ij} couplings extracted through such in-field experiment would be significantly renormalized compared to the bare J_{ij} needed to describe the zero-field specific heat and neutron scattering data? To address this issue, we first note that with an excited crystal-field doublet at an energy of order 300 K above the ground-state doublet, one can safely neglect the field-induced admixing between the ground doublet and excited doublet for a [112] field of order of 2 T. This field strength corresponds to a Zeeman splitting of about 20 K for a magnetic moment of 10 μ_B (ignoring geometrical factors arising from projection of the local ⟨111⟩ Ising direction of the spins on the triangular layer with the [112] direction). Second, as the g tensor for the crystal-field Dy^{3+} ion in $Dy_2Ti_2O_7$ is strictly Ising type [15], the projection of the microscopic interionic Hamiltonian into the crystal-field doublet would not be modified by field-induced perturbative corrections to the crystal-field ground-state doublet wave functions. Finally, one notes that in the case of the Er^{3+} and Yb^{3+} Kramers ions in $Er_2Ti_2O_7$ and $Yb_2Ti_2O_7$, the anisotropic spin-spin coupling parameters describing the interactions between all the components of the effective $\boldsymbol{S} = \frac{1}{2}$ spin determined in large magnetic field [71,72] can be successfully used to describe, without any adjustable parameters or field-induced renormalization of the couplings, the zero-field properties of these compounds [73–75]. On the basis of those three arguments, we would thus expect that the constrained J_{ij} parameters for $Dy_2Ti_2O_7$ determined in a [112] field of 2 T do not suffer from important field-induced renormalization compared to the zero-field values that we ultimately seek.

APPENDIX B: PHASE DIAGRAM CALCULATIONS

In order to determine the possible ordered state(s) that may arise in the system, we first apply mean-field theory [48] and then carry out Monte Carlo simulations. We employ mean-field theory to perform a general survey of the entire parameter range and follow up with a direct inspection of the low-temperature ordered states found in the Monte Carlo calculation.

Considering the entire Brillouin zone, we find the mean-field ordering wave vector to be in the $(hk0)$ plane for the entire parameter space relevant for for $Dy_2Ti_2O_7$, namely,

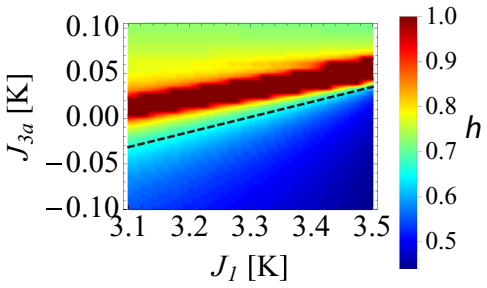

FIG. 12. Mean-field ordering wave vector. Map of the mean-field ordering wave vector $\boldsymbol{q}$ in the constrained J_1-J_{3a} parameter space, where the system selects a wave vector along the $(hh0)$ direction. The broad red band across the middle indicates the single-chain phase with $\boldsymbol{q} = (1\ 1\ 0)$. In the lower part of the figure, the order is close to the double-chain ordering wave vector $\boldsymbol{q} = (\frac{1}{2}\ \frac{1}{2}\ 0)$. The phase boundary according to Eq. (6) is shown as a dashed black line.

$3.1\ \text{K} < J_1 < 3.5\ \text{K}$ and $-0.1\ \text{K} < J_{3a} < 0.1$ K. We also find that $h = k$ and show in Fig. 12 the mean-field ordering wave vector at the mean-field critical temperature T_c^{MF} along the $(hh0)$ direction as a function of J_1 and J_{3a}. We note a horizontal band of (1 1 0) order below which there is a gradual shift through incommensurate h values to, ultimately, a region with ordering at $(\frac{1}{2}\ \frac{1}{2}\ 0)$. At this point, it is important to realize that the equal-moment constraint does not apply to the mean-field theory, but limits the admissible ordering wave vectors of the real material and our model. Furthermore, we note that this constraint applies also to states with mean-field ordering wave vectors that are commensurate with the Monte Carlo simulation cells, such as, for example, a wave vector $(\frac{3}{4}\ \frac{3}{4}\ 0)$ (Ref. [76]). Inspecting the low-temperature states in the Monte Carlo simulation we find that the gradual shift from ordering wave vector (1 1 0) to $(\frac{1}{2}\ \frac{1}{2}\ 0)$, observed at T_c^{MF} in mean-field theory, is replaced by a direct transition between these two ordered states, as illustrated in Fig. 3. We now discuss the nature of the two phases with ground-state ordering wave vectors (1 1 0) and $(\frac{1}{2}\ \frac{1}{2}\ 0)$ found in the Monte Carlo simulations. These correspond to the upper and lower basins of Figs. 5(c) and 5(d) in the main text, respectively. We first focus on the ordered structures at $T = 0$ before considering finite-temperature behavior.

As previously found for the simple dipolar spin ice model with $J_2 = J_{3a} = J_{3b} = 0$ (Ref. [22]), the state at (1 1 0), or equivalently (0 0 1), corresponds to the "single-chain" state. In this state, parallel chains of spins order antiferromagnetically when viewed along a cubic ⟨100⟩ axis [see Fig. 13(a)]. Inspection of the Monte Carlo spin configuration of the novel state with propagation vector $(\frac{1}{2}\ \frac{1}{2}\ 0)$ reveals a pattern where *pairs* of adjacent chains have spins aligned parallel but pointing in the opposite direction of the adjacent pairs on either side [see Fig. 13(b)]. This period doubling in the x-y plane is the direct space origin of why the ordering wave vector is reduced from (1 1 0) to $(\frac{1}{2}\ \frac{1}{2}\ 0)$. We thus refer to this as the "double-chain" state.

To gain a better understanding of how the competition between these two states arises from third-nearest-neighbor interactions [77], we invoke yet another description of the

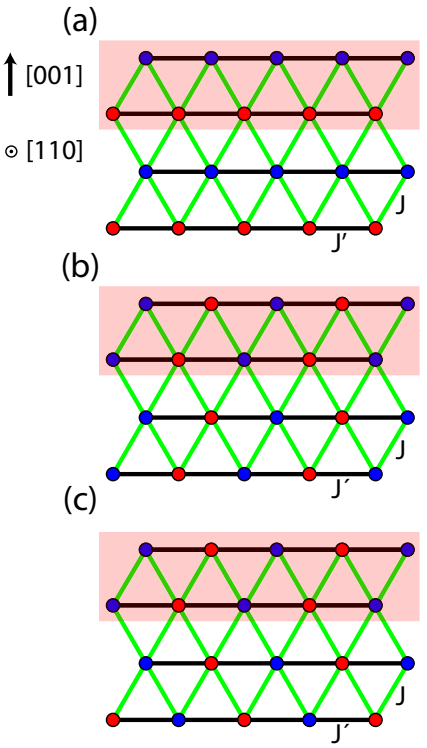

FIG. 13. Spin configuration in the ordered state. View along spin chains in the [110] direction. A red circle denotes an entire, ferromagnetically ordered, chain pointing out of the page, while a blue circle denotes a chain pointing into the page. A black bond segment indicates an exchange coupling $J' = J_{3b}$ while a green bond segment denotes coupling $J = J_{3a} + J_{3b} + J_2/3$. The semitransparent red bar indicates a layer of spin chains, commonly viewed along the [001] direction, such as in Figs. 1(f) and 1(g) of the main text. The single-chain state is shown in (a), while a double-chain long-range-ordered state is depicted in (b). An example of a random stacking of the double-chain state is shown in (c).

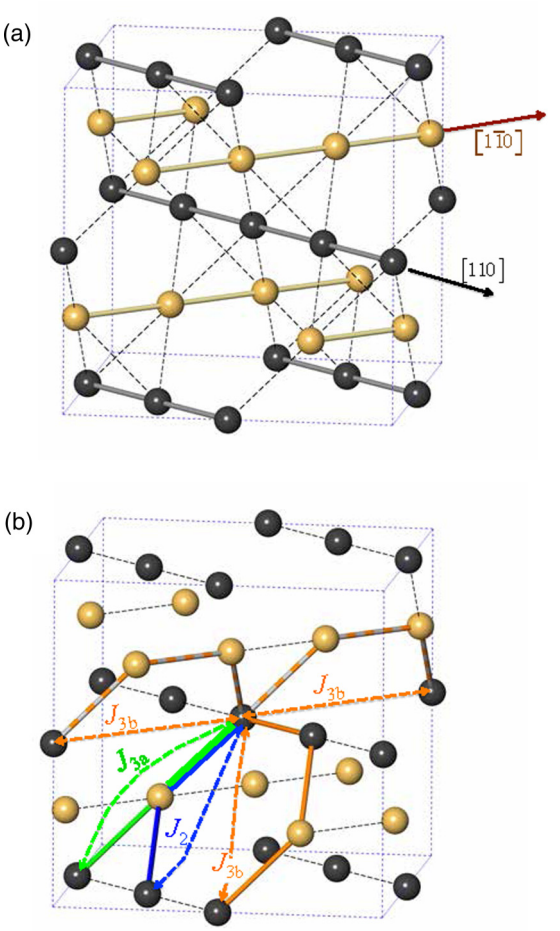

FIG. 14. Spin chains. (a) The pyrochlore lattice is represented as a collection of spin chains along the [110] (black atoms and bonds) and [1$\bar{1}$0] (yellow atoms and bonds) directions. Dashed black bonds couple different chains together. (b) Further-neighbor interactions J_2 (blue dashed line), J_{3a} (green dashed line), and J_{3b} (orange dashed line) couple different [110] chains together. Two neighboring chains in the same (001) plane are coupled by $J' \equiv J_{3b}$ (per spin) while a pair of neighboring chains on two adjacent (001) planes are coupled by $J \equiv J_{3a} + J_{3b} + J_2/3$ (per spin).

magnetic sites of the pyrochlore lattice. After having viewed it as a collection of alternating kagome and triangular layers in the previous section, we now view it as an array of two sets of one-dimensional spin chains along the [110] and [1$\bar{1}$0] directions [see Fig. 14(a)]. In the long-ranged-ordered states observed in the Monte Carlo simulation the spins on each individual [110] and [1$\bar{1}$0] chains are ferromagnetically correlated, and we therefore treat these chains as elementary units. In a plane perpendicular to the respective direction of the chains, the two sets of chains form two triangular lattices, which are decoupled from each other if only exchange couplings J_1, J_2, J_{3a}, and J_{3b} are considered. Therefore, we first consider a triangular lattice formed by spin chains along the [110] direction and ignore (for the moment) the long-range dipolar interactions. Each chain couples to two of its nearest neighbors with the same z coordinate with exchange coupling $J' = J_{3b}$, while the chain couples to the other four nearest neighbors with exchange coupling $J = J_{3a} + J_{3b} + J_2/3$, as illustrated in Figs. 13 and 14(b). Both couplings are determined using the convention used in Ref. [36] with $\hat{z}_i \cdot \hat{z}_j$ explicitly included. As stated above, two third-neighbor coupled sites belong to the same sublattice with $\hat{z}_i \cdot \hat{z}_j = 1$, while two second-neighbor sites reside on two different sublattices so that $\hat{z}_i \cdot \hat{z}_j = -\frac{1}{3}$. The negative sign does not appear in the definition of J thanks to an additional negative sign coming from the alternating directions of spins, represented in their local components along $\hat{z}_i$, along a "ferromagnetically" ordered chain in the global [110] direction. In summary, the (001) planes of [110] spin chains have intraplane nearest-neighbor coupling J' and interplane coupling J.

We thus end up mapping the competing states observed in the Monte Carlo simulations of the three-dimensional pyrochlore lattice to a two-dimensional triangular lattice, for which the ground-state phase diagram can be obtained by straightforward energy arguments. For $J' < J$, the planes of spin chains form ferromagnetic sheets whose directions alternate between planes. This state corresponds to the single-chain phase [Fig. 13(a)]. For $J' > J$, the [110] spin chains within the same (001) plane form an antiferromagnetic

state, corresponding to the double-chain state [Fig. 13(b)]. The interplane coupling is frustrated and these planes are decoupled with different stackings of the antiferromagnetic planes being degenerate [Fig. 13(c)]. Moreover, due to the antiferromagnetic ordering of the spin chains within a given (001) plane, the long-range dipolar interaction is well shielded for an arbitrary stacking of the planes (i.e., with a propagation vector along [001]). In Fig. 13, the structure of the single- and double-chain states is shown from the spin-chain perspective.

The boundary between the two phases is determined by the condition $J = J'$ if the long-range dipolar interaction is not included. The dipolar interaction D shifts the boundary marginally by a small constant. By determining this constant numerically using the Ewald summation method, we obtain Eq. (6) for the boundary:

$$J_{3a} + \frac{J_2}{3} + 0.02D = 0. \tag{B1}$$

This equation, in combination with Eq. (5), was used to draw the phase boundary in Figs. 4(b) and 5(a)–5(d) as well as for Figs. 12 and 17. Note the small 0.02 prefactor in front of the dipolar contribution term D, which *a posteriori* justifies the discussion above in terms of approximately independent sets of [110] and [1$\bar{1}$0] chains.

Finally, we consider some experimentally observable finite-temperature consequences of the stacking degeneracy of the double-chain state. From Figs. 4(f)–4(h) it is clear that the signature of the double-chain phase in the Monte Carlo calculation of the neutron scattering $S(\boldsymbol{q})$ occurs at $(\frac{1}{2}\ \frac{1}{2}\ \frac{1}{2})$, and not at the mean-field ordering wave vector $(\frac{1}{2}\ \frac{1}{2}\ 0)$. In order to rationalize the temperature evolution of $S(\boldsymbol{q})$ we again first turn to a mean-field analysis. In Fig. 15, we show $S(\boldsymbol{q})$ calculated in mean-field theory at $J_1 = 3.41$ K and $J_{3a} = -0.04$ K, a point deep in the double-chain region. The temperature is expressed in terms of the critical mean-field temperature $T_c^{\mathrm{MF}} = 2.9614$ K, for these (J_1, J_{3a}) values. Note how the main response stays at $(\frac{1}{2}\ \frac{1}{2}\ \frac{1}{2})$ until extremely close to the transition temperature $T = 1.0001 T_c^{\mathrm{MF}}$, where the weight finally shifts to the ordering wave vector $(\frac{1}{2}\ \frac{1}{2}\ 0)$. The true order parameter is therefore effectively hidden by the near degeneracy of different stackings in the z direction down to very close to the transition temperature. In the Monte Carlo simulation, the ordering proceeds in a different manner. At high temperature, the Monte Carlo results for $S(\boldsymbol{q})$ agree perfectly with mean-field theory as it should [48]. Below $T \approx 10\, T_c^{\mathrm{MF}}$, differences start to emerge. At the transition temperature $T_c^{\mathrm{MC}} \sim 0.13$ K, the Monte Carlo system freezes into a state of long-range order in the x-y (110) plane, but with random stacking in the ([001]) z direction [see Fig. 13(c)]. Only by using parallel tempering Monte Carlo methods with a very fine-temperature mesh (see Sec. II B) could the true perfectly stacked double-chain ground state [Fig. 13(b)] be resolved in the simulation performed with 1024 ($L = 4$) spins.

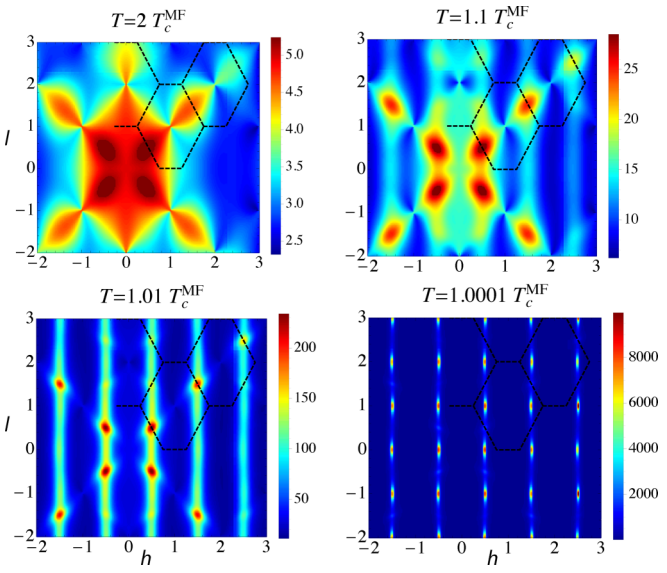

FIG. 15. Mean-field neutron scattering structure factor $\boldsymbol{S(q)}$ in the double-chain region. The various panels show the structure factor $S(\boldsymbol{q})$ in the (hhl) plane calculated in mean-field theory as the mean-field critical temperature $T_c^{\mathrm{MF}} = 2.9614$ K is approached from the paramagnetic phase for the set of constrained exchange couplings with $J_1 = 3.41$ K and $J_{3a} = -0.04$ K, a point deep in the double-chain region in the phase diagram of Fig. 12. The weight shifts from $(\frac{1}{2}\ \frac{1}{2}\ \frac{1}{2})$ to the true ordering wave vector $(\frac{1}{2}\ \frac{1}{2}\ 0)$ at $T = 1.0001\, T_c^{\mathrm{MF}}$, extremely close to the transition temperature.

APPENDIX C: NEUTRON SCATTERING ANALYSIS

We begin by analyzing how a possible freezing of the sample would affect the neutron scattering structure factor $S(\boldsymbol{q})$. From numerous experiments, is is clear that thermal equilibration is adequately fast above 0.7 K, while the samples rapidly fall out of equilibrium below that temperature [30,33,34]. Considering the typical time duration of neutron scattering data accumulation at a given temperature ($\sim 10^0$–10^1 h) we assume that the experimental neutron scattering data were well equilibrated down to 0.7 K, while below this temperature we cannot say with certainty whether the sample was fully equilibrated, partially equilibrated, or frozen.

The effects of freezing can be explored in a Monte Carlo simulation. Below 0.7 K, the number of single spin flips required to equilibrate the sample increases exponentially and loop updates are generally needed to speed up the thermalization [22,23]. We thus study the effects of freezing by measuring $S(\boldsymbol{q})$ at successively lower temperatures by using *only* single spin-flip updates and keeping the number of updates at each temperature constant to mimic a fixed experimental equilibration time scale. To this end, we use 10^5 MC steps at each temperature. With this choice, the simulated system effectively freezes slightly below a temperature of 0.6 K. In Fig. 16, we display $S(\boldsymbol{q})$ where the columns represent $T = 0.7$, 0.5, and 0.3 K, moving left to right. The first, second, and fourth rows represent a parameter point in the single-chain region, on the boundary, and in the double-chain region, respectively. One clearly sees that, as the system freezes, as assessed by the vanishing Monte Carlo spin-flip rate (not shown), the neutron scattering pattern also freezes. Most importantly, there is *no change* in the ZBS and *no* fundamental reciprocal space redistribution in the peak intensities. We therefore conclude that the pattern recorded at $T = 0.3$ K looks like the pattern at the last temperature the sample was properly

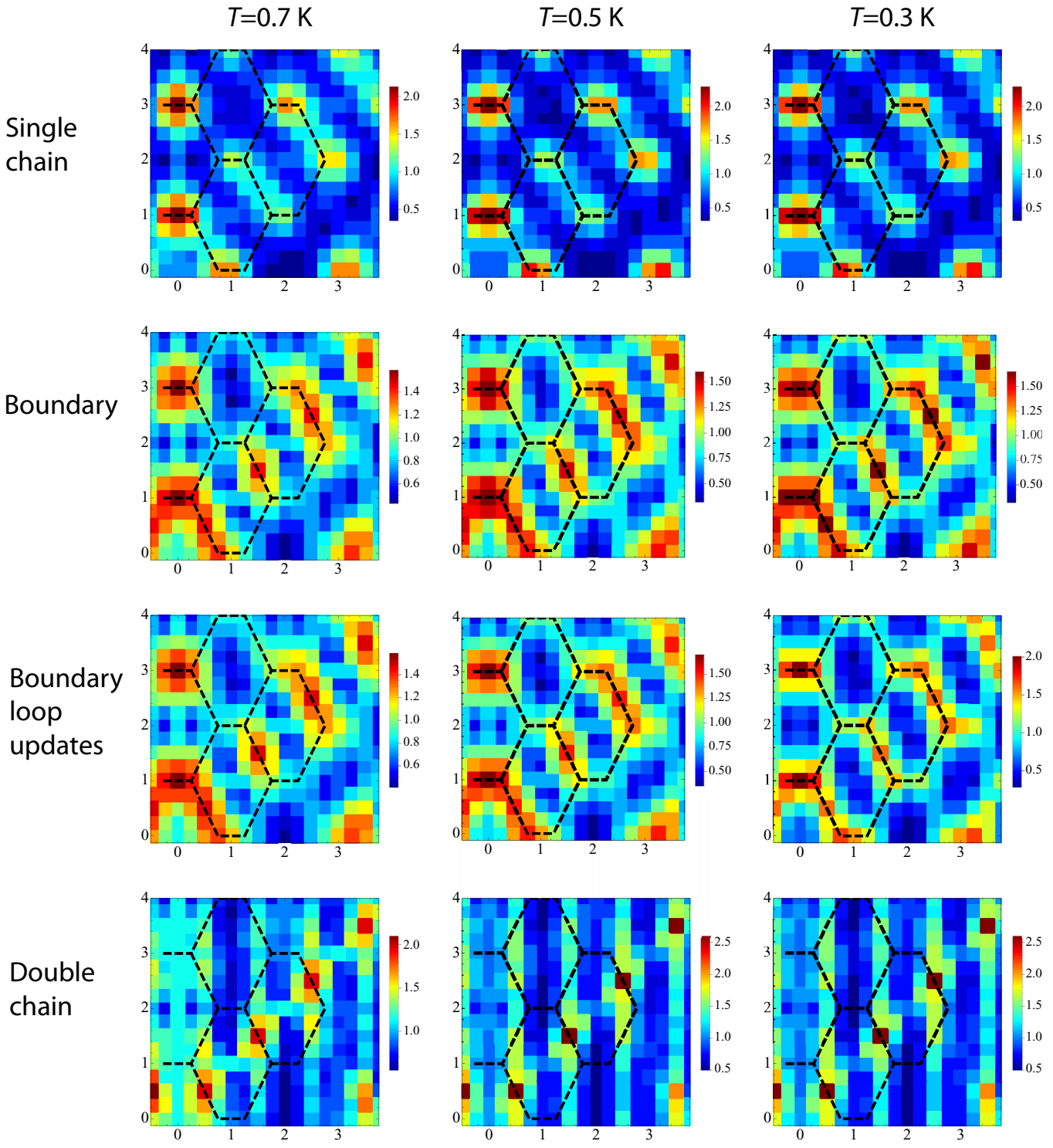

FIG. 16. Simulation of structure factor as the system freezes. Simulation of neutron structure factor using 10^5 MC steps consisting of only attempted single spin flips for a system of 1024 spins ($L = 4$). The three columns stand for $T = 0.7$, 0.5, and 0.3 K. The top row represents a point in the single-chain region ($J_1 = 3.3$ K, $J_{3a} = 0.07$ K), the second row a point close to the boundary ($J_1 = 3.41$ K, $J_2 = -0.14$ K, $J_{3a} = J_{3b} = 0.025$ K, Ref. [36]), and the bottom row a point in the double-chain region ($J_1 = 3.44$ K, $J_{3a} = -0.02$ K). Only few updates are accepted below $T = 0.6$ K causing little further change in the structure factor below this temperature. This indicates that the structure factor in a frozen material is an imprint of the pattern at the temperature at which the sample froze. The third row represents the same parameter point as the second row, but now with loop updates employed to achieve complete equilibration at all temperatures. Also in this case the scattering patterns at $T = 0.5$ and 0.3 K are quite similar. The displayed structure factor in the first, second, and last rows is an average over 400 different simulations that have frozen in different configurations, modeling the spatial variations in a macroscopic sample used in the experiments and which neutron scattering measurements average out.

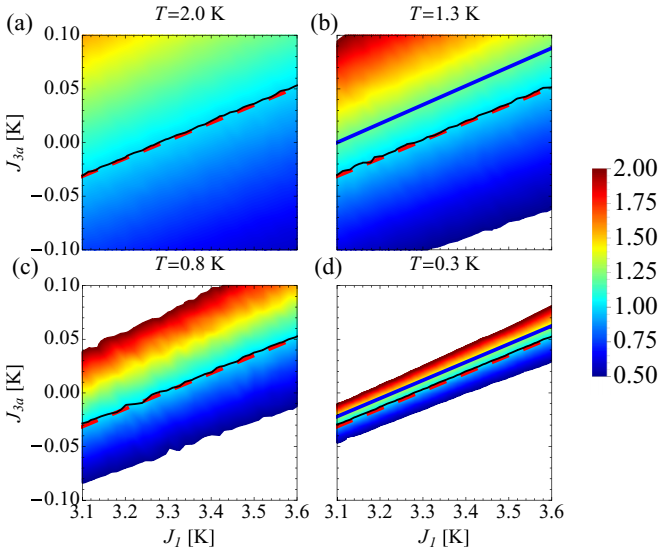

FIG. 17. Ratio of structure factor for single-chain and double-chain order. The ratio $r \equiv S(0\ 0\ 3)/S(\frac{3}{2}\ \frac{3}{2}\ \frac{3}{2})$ in the constrained J_1-J_{3a} plane calculated in the Monte Carlo simulations, without the Dy^{3+} form factor. The phase boundary is marked by a dashed red line, and the $r = 1$ contour is indicated by a thin black line, which overlaps the phase boundary in all panels. For all temperatures, the ratio is therefore unity at the phase boundary, while it is greater than one in the single-chain region above the boundary and less than one in the double-chain region below the boundary. The blue lines in (b) and (d) indicate the ratio for the experimental neutron scattering data at $T = 1.3$ and 0.3 K.

thermally equilibrated, independently of the dynamical state of the experimental data nominally measured at 0.3 K.

Next, we perform a more detailed analysis of the intensity maxima in the structure factor. As noted in the main text, the single-chain phase neutron scattering response $S(\boldsymbol{q})$ occurs at the ordering wave vector (1 1 0) or, equivalently, at (0 0 3) in the experimental neutron scattering data where the second Brillouin zone is probed. On the other hand, the double-chain phase response occurs at the ordering wave vector $(\frac{1}{2}\ \frac{1}{2}\ \frac{1}{2})$, or equivalently $(\frac{3}{2}\ \frac{3}{2}\ \frac{3}{2})$ in the experiments, rather than at $(\frac{1}{2}\ \frac{1}{2}\ 0)$ because of the aforementioned random stacking of ordered spin planes. In order to quantify this observation, we show in Fig. 17 the ratio $r \equiv S(0\ 0\ 3)/S(\frac{3}{2}\ \frac{3}{2}\ \frac{3}{2})$ at temperatures $T = 2.0$, 1.3, 0.8, and 0.3 K (without the Dy^{3+} magnetic form factor) computed using Monte Carlo simulations. Interestingly, r is precisely unity at the boundary determined by Eq. (6) and is shown as a dashed red line in the four panels of Fig. 17. In the single-chain region, above the phase boundary, $r > 1$, while $r < 1$ in the double-chain region *independently* of the temperature. The experimental ratio, after dividing out the Dy^{3+} form factor, is $r \cong 1.18$ at $T = 1.3$ K and $r \cong 1.29$ at $T = 0.3$ K and is marked by a dark blue line in Figs. 17(b) and 17(d), respectively. The present neutron scattering experiments therefore position $Dy_2Ti_2O_7$ very close to, but slightly above, the ground-state phase boundary line, that is in the single-chain region of the phase diagram. Note that the experimental ratio at $T = 0.3$ K locates $Dy_2Ti_2O_7$ closer to the phase boundary than does the ratio at $T = 1.3$ K. However, small differences in the measured value of r have a large effect on the position of the corresponding contour line in Fig. 17(d). To determine the location of $Dy_2Ti_2O_7$ in the phase diagram with high precision, one would need a sequence of high-resolution and well-equilibrated experimental neutron scattering measurements of $S(\boldsymbol{q})$ at several temperatures between 0.3 and 1.3 K. Also, note the remarkable implication of the analysis above: neutron scattering experiments performed at a high temperature allows one to "anticipate" the ground state of the material (excluding quantum, and other disruptive low-T phenomena) simply by analyzing the peak ratio r.

APPENDIX D: NUCLEAR SPECIFIC HEAT

Whereas it is common knowledge that the nuclear contribution dominates over the electronic part of the specific heat of holmium-based compounds at $T \lesssim 1.5$ K [58–60], the nuclear specific heat of $Dy_2Ti_2O_7$ has generally been ignored. Here, we show that, for a quantitative analysis, this is not justified below $T \approx 0.5$ K. Since the main nuclear contribution to the specific heat comes from the interaction of the deep-lying $4f$ electrons and the nucleus, this interaction is considered not to be directly affected by the ionic environment [78]. While the crystal field can alter the symmetry of the crystal-field doublet, one expects that if the magnitude and symmetry of the moment $\langle J^z \rangle$ are similar in two different compounds, the effective hyperfine field $A\langle J^z \rangle$ interaction should be expected to be roughly the same. In $Dy_2Ti_2O_7$, the Ising [47] magnetic moment of each ion is nearly saturated, with $\langle J^z \rangle \approx 7.4$, which is close to the $J = \frac{15}{2}$ value for Dy^{3+}. We therefore use the results of a calorimetric investigation of the nuclear interactions in metallic Dy, which also has a fully developed electronic moment [78]. Following this investigation we write the nuclear hyperfine (hf) Hamiltonian as

$$H_{\rm hf} = \tilde{A} I^z + P\left[(I^z)^2 - \tfrac{1}{3} I(I+1)\right], \qquad \text{(D1)}$$

with $\tilde{A} \equiv A\langle J^z \rangle$ where A and P are the contact hyperfine term and electric quadrupole constants, respectively. Assuming the

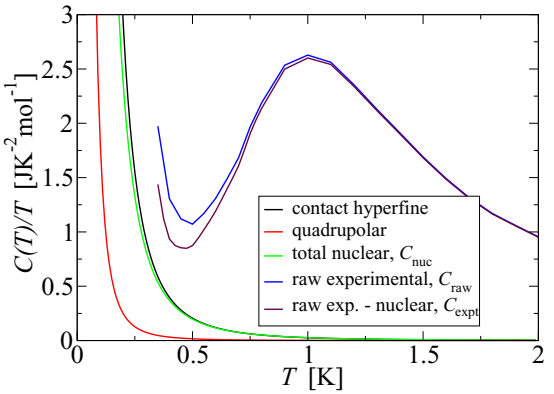

FIG. 18. Nuclear contact contribution (black curve), quadrupolar (red curve), and total $C_{\rm nuc}/T$ (green curve) nuclear contribution to the specific heat. The blue curve shows the raw experimental $C_{\rm raw}/T$ data while the purple curves shows the residual electronic data $C_{\rm expt}(T)/T$ data.

natural abundance of Dy, the relevant magnetic isotopes are 18.88% ^{161}Dy and 24.97% ^{163}Dy, both with nuclear spin $I = \frac{5}{2}$. We use the parameters $\tilde{A}_{161} = 0.0399$ K, $P_{161} = 0.0093$ K, $\tilde{A}_{163} = 0.0559$ K, and $P_{163} = 0.0098$ K from Ref. [78]. These values are also roughly ($\pm 10\%$) from those determined in various Dy-based insulating salts [62,79–82]. The hyperfine partition function is given by $Z_{\rm hf} = \sum_{I^z=-5/2}^{I^z=+5/2} e^{-\beta H_{\rm hf}}$, and the calculation of the nuclear contribution to the specific heat is straightforward. The result is shown in Fig. 18, where we display the total nuclear specific heat as well as the separate contact hyperfine and electric quadrupolar terms. Notice that the electric quadrupolar term, which becomes somewhat noticeable below $T \approx 0.2$ K, *reduces* the total nuclear contribution. It is clear that there is a significant nuclear contribution to the total $C_{\rm raw}(T)/T$ specific heat below $T \approx 0.5$ K, and the nuclear specific heat causes part of the shoulder that starts to develop already at $T \approx 0.7$ K. Given this non-negligible hyperfine contribution, it would be very interesting to see the result of a well-equilibrated measured specific-heat measurement on a ^{162}Dy enriched sample used for neutron scattering studies [33,40,55] since there should be no nuclear specific heat for such a sample.

[1] *Highly Frustrated Magnetism*, edited by C. Lacroix, P. Mendels, and F. Mila, Springer Series in Solid-State Sciences, Vol. 164 (Springer, Berlin, 2011).

[2] J. S. Gardner, M. J. P. Gingras, and J. E. Greedan, Magnetic pyrochlore oxides, Rev. Mod. Phys. **82**, 53 (2010).

[3] L. Balents, Spin liquids in frustrated magnets, Nature (London) **464**, 199 (2010).

[4] P. W. Anderson, The resonating valence bond state in La_2CuO_4 and superconductivity, Science **235**, 1196 (1987).

[5] M. J. P. Gingras and P. A. McClarty, Quantum spin ice: a search for gapless quantum spin liquids in pyrochlore magnets, Rep. Prog. Phys. **77**, 056501 (2014).

[6] P. Chandra and B. Doucot, Possible spin-liquid state at large s for the frustrated square Heisenberg lattice, Phys. Rev. B **38**, 9335 (1988).

[7] R. Melzi, P. Carretta, A. Lascialfari, M. Mambrini, M. Troyer, P. Millet, and F. Mila, $Li_2VO(Si,Ge)O_4$, a Prototype of a Two-Dimensional Frustrated Quantum Heisenberg Antiferromagnet, Phys. Rev. Lett. **85**, 1318 (2000).

[8] A. Bombardi, J. Rodriguez-Carvajal, S. Di Matteo, F. de Bergevin, L. Paolasini, P. Carretta, P. Millet, and R. Caciuffo, Direct Determination of the Magnetic Ground State in the Square Lattice $S = 1/2$ Antiferromagnet Li_2VOSIO_4, Phys. Rev. Lett. **93**, 027202 (2004).

[9] B. Fåk, E. Kermarrec, L. Messio, B. Bernu, C. Lhuillier, F. Bert, P. Mendels, B. Koteswararao, F. Bouquet, J. Ollivier, A. D. Hillier, A. Amato, R. H. Colman, and A. S. Wills, Kapellasite: A Kagome Quantum Spin Liquid with Competing Interactions, Phys. Rev. Lett. **109**, 037208 (2012).

[10] J. N. Reimers, A. J. Berlinsky, and A.-C. Shi, Mean-field approach to magnetic ordering in highly frustrated pyrochlores, Phys. Rev. B **43**, 865 (1991).

[11] R. Moessner and J. T. Chalker, Low-temperature properties of classical geometrically frustrated antiferromagnets, Phys. Rev. B **58**, 12049 (1998).

[12] M. J. P. Gingras and B. C. den Hertog, Origin of spin-ice behavior in Ising pyrochlore magnets with long-range dipole interactions: an insight from mean-field theory, Can. J. Phys. **79**, 1339 (2001).

[13] J. Villain, Insulating spin glasses, Z. Phys. B: Condens. Matter Quanta **33**, 31 (1979).

[14] A. Sen, K. Damle, and R. Moessner, Fractional Spin Textures in the Frustrated Magnet $SrCr_{9p}Ga_{12-9p}O_{19}$, Phys. Rev. Lett. **106**, 127203 (2011).

[15] M. J. P. Gingras, Spin ice, in *Highly Frustrated Magnetism*, Springer Series in Solid-State Sciences, Vol. 164, edited by C Lacroix, P Mendels, and F Mila (Springer, Berlin, 2011).

[16] S. T. Bramwell and M. J. P. Gingras, Spin ice state in frustrated magnetic pyrochlore materials, Science **294**, 1495 (2001).

[17] M. J. Harris, S. T. Bramwell, D. F. McMorrow, T. Zeiske, and K. W. Godfrey, Geometrical Frustration in the Ferromagnetic Pyrochlore $Ho_2Ti_2O_7$, Phys. Rev. Lett. **79**, 2554 (1997).

[18] A. P. Ramirez, A. Hayashi, R. J. Cava, R. Siddharthan, and B. S. Shastry, Zero-point entropy in 'spin ice', Nature (London) **399**, 333 (1999).

[19] R. Siddharthan, B. S. Shastry, A. P. Ramirez, A. Hayashi, R. J. Cava, and S. Rosenkranz, Ising Pyrochlore Magnets: Low-Temperature Properties, "Ice Rules," and Beyond, Phys. Rev. Lett. **83**, 1854 (1999).

[20] B. C. den Hertog and M. J. P. Gingras, Dipolar Interactions and Origin of Spin Ice in Ising Pyrochlore Magnets, Phys. Rev. Lett. **84**, 3430 (2000).

[21] S. V. Isakov, R. Moessner, and S. L. Sondhi, Why Spin Ice Obeys the Ice Rules, Phys. Rev. Lett. **95**, 217201 (2005).

[22] R. G. Melko, B. C. den Hertog, and M. J. P. Gingras, Long-Range Order at Low Temperatures in Dipolar Spin Ice, Phys. Rev. Lett. **87**, 067203 (2001).

[23] R. G. Melko and M. J. P. Gingras, Monte Carlo studies of the dipolar spin ice model, J. Phys.: Condens. Matter **16**, R1277 (2004).

[24] M. J. Harris, S. T. Bramwell, T. Zeiske, D. F. McMorrow, and P. J. C. King, Magnetic structures of highly frustrated pyrochlores, J. Magn. Magn. Mater. **177–181**, 757 (1998).

[25] H. Fukazawa, R. G. Melko, R. Higashinaka, Y. Maeno, and M. J. P. Gingras, Magnetic anisotropy of the spin-ice compound $Dy_2Ti_2O_7$, Phys. Rev. B **65**, 054410 (2002).

[26] C. Castelnovo, R. Moessner, and S. L. Sondhi, Magnetic monopoles in spin ice, Nature (London) **451**, 42 (2008).

[27] C. Castelnovo, R. Moessner, and S. L. Sondhi, Thermal Quenches in Spin Ice, Phys. Rev. Lett. **104**, 107201 (2010).

[28] C. Paulsen, M. J. Jackson, E. Lhotel, B. Canals, D. Prabhakaran, K. Matsuhira, S. R. Giblin, and S. T. Bramwell, Far-from-equilibrium monopole dynamics in spin ice, Nat. Phys. **10**, 135 (2014).

[29] H. M. Revell, L. R. Yaraskavitch, J. D. Mason, K. A. Ross, H. M. L. Noad, H. A. Dabkowska, B. D. Gaulin, P. Henelius, and J. B. Kycia, Evidence of impurity and boundary effects on magnetic monopole dynamics in spin ice, Nat. Phys. **9**, 34 (2013).

[30] D. Pomaranski, L. R. Yaraskavitch, S. Meng, K. A. Ross, H. M. L. Noad, H. A. Dabkowska, B. D. Gaulin, and J. B. Kycia, Absence of Pauling's residual entropy in thermally equilibrated $Dy_2Ti_2O_7$, Nat. Phys. **9**, 353 (2013).

[31] G. Sala, M. J. Gutmann, D. Prabhakaran, D. Pomaranski, C. Mitchelitis, J. B. Kycia, D. G. Porter, C. Castelnovo, and J. P. Goff, Vacancy defects and monopole dynamics in oxygen-deficient pyrochlores, Nat. Mater. **13**, 488 (2014).

[32] H. D. Zhou, J. G. Cheng, A. M. Hallas, C. R. Wiebe, G. Li, L. Balicas, J. S. Zhou, J. B. Goodenough, J. S. Gardner, and E. S. Choi, Chemical Pressure Effects on Pyrochlore Spin Ice, Phys. Rev. Lett. **108**, 207206 (2012).

[33] B. Klemke, M. Meissner, P. Strehlow, K. Kiefer, S. A. Grigera, and D. A. Tennant, Thermal relaxation and heat transport in the spin ice material $Dy_2Ti_2O_7$, J. Low Temp. Phys. **163**, 345 (2011).

[34] R. Higashinaka, H. Fukazawa, D. Yanagishima, and Y. Maeno, Specific heat of $Dy_2Ti_2O_7$ in magnetic fields: comparison between single-crystalline and polycrystalline, J. Phys. Chem. Solids **63**, 1043 (2002).

[35] Y. Tabata, H. Kadowaki, K. Matsuhira, Z. Hiroi, N. Aso, E. Ressouche, and B. Fåk, Kagome Ice State in the Dipolar Spin Ice $Dy_2Ti_2O_7$, Phys. Rev. Lett. **97**, 257205 (2006).

[36] T. Yavors'kii, T. Fennell, M. J. P. Gingras, and S. T. Bramwell, $Dy_2Ti_2O_7$ Spin Ice: A Test Case for Emergent Clusters in a Frustrated Magnet, Phys. Rev. Lett. **101**, 037204 (2008).

[37] J. P. C. Ruff, R. G. Melko, and M. J. P. Gingras, Finite-Temperature Transitions in Dipolar Spin Ice in a Large Magnetic Field, Phys. Rev. Lett. **95**, 097202 (2005).

[38] R. Higashinaka and Y. Maeno, Field-Induced Transition on a Triangular Plane in the Spin-Ice Compound $Dy_2Ti_2O_7$, Phys. Rev. Lett. **95**, 237208 (2005).

[39] H. Sato, K. Matsuhira, T. Tayama, Z. Hiroi, S. Takagi, and T. Sakakibara, Ferromagnetic ordering on the triangular lattice in the pyrochlore spin-ice compound $Dy_2Ti_2O_7$, J. Phys.: Condens. Matter **18**, L297 (2006).

[40] T. Fennell, O. A. Petrenko, B. Fåk, S. T. Bramwell, M. Enjalran, T. Yavors'kii, M. J. P. Gingras, R. G. Melko, and G. Balakrishnan, Neutron scattering investigation of the spin ice state in $Dy_2Ti_2O_7$, Phys. Rev. B **70**, 134408 (2004).

[41] P. A. McClarty, O. Sikora, R. Moessner, K. Penc, F. Pollmann, and N. Shannon, Chain-based order and quantum spin liquids in dipolar spin ice, Phys. Rev. B **92**, 094418 (2015).

[42] K. A. Ross, Th. Proffen, H. A. Dabkowska, J. A. Quilliam, L. R. Yaraskavitch, J. B. Kycia, and B. D. Gaulin, Lightly stuffed pyrochlore structure of single-crystalline $Yb_2Ti_2O_7$ grown by the optical floating zone technique, Phys. Rev. B **86**, 174424 (2012).

[43] Kristen Baroudi, Bruce D. Gaulin, Saul H. Lapidus, Jonathan Gaudet, and R. J. Cava, Symmetry and light stuffing of $Ho_2Ti_2O_7$, $Er_2Ti_2O_7$, and $Yb_2Ti_2O_7$ characterized by synchrotron x-ray diffraction, Phys. Rev. B **92**, 024110 (2015).

[44] Z. Hao, A. G. R. Day, and M. J. P. Gingras, Bosonic many-body theory of quantum spin ice, Phys. Rev. B **90**, 214430 (2014).

[45] Y. Kato and S. Onoda, Numerical Evidence of Quantum Melting of Spin Ice: Quantum-Classical Crossover, Phys. Rev. Lett **115**, 077202 (2015).

[46] P. Santini, S. Carretta, G. Amoretti, R. Caciuffo, N. Magnani, and G. H. Lander, Multipolar interactions in f-electron systems: The paradigm of actinide dioxides, Rev. Mod. Phys. **81**, 807 (2009).

[47] J. G. Rau and M. J. P. Gingras, Magnitude of quantum effects in classical spin ices, Phys. Rev. B **92**, 144417 (2015).

[48] M. Enjalran and M. J. P. Gingras, Theory of paramagnetic scattering in highly frustrated magnets with long-range dipole-dipole interactions: The case of the $Tb_2Ti_2O_7$ pyrochlore antiferromagnet, Phys. Rev. B **70**, 174426 (2004).

[49] E. Marinari and G. Parisi, Simulated Tempering: A New Monte Carlo Scheme, Europhys. Lett. **19**, 451 (1992).

[50] P. J. Brown, International tables for crystallography, in *International Tables for Crystallography*, Vol. C, edited by A. J. C. Wilson (D. Reidel, Dordrecht, Holland, 1983-1993), Chap. 4.4.5, p. 391.

[51] W. Selke, The ANNNI model – theoretical analysis and experimental application, Phys. Rep. **170**, 213 (1988).

[52] C. L. Henley, The coulomb phase in frustrated systems, Annu. Rev. Condens. Matter Phys. **1**, 179 (2010).

[53] A. Sen, R. Moessner, and S. L. Sondhi, Coulomb Phase Diagnostics as a Function of Temperature, Interaction Range, and Disorder, Phys. Rev. Lett. **110**, 107202 (2013).

[54] T. Fennell, P. P. Deen, A. R. Wildes, K. Schmalzl, D. Prabhakaran, A. T. Boothroyd, R. J. Aldus, D. F. McMorrow, and S. T. Bramwell, Magnetic Coulomb phase in the spin ice $Ho_2Ti_2O_7$, Science **326**, 415 (2009).

[55] D. J. P. Morris, D. A. Tennant, S. A. Grigera, B. Klemke, C. Castelnovo, R. Moessner, C. Czternasty, M. Meissner, K. C. Rule, J.-U. Hoffmann, K. Kiefer, S. Gerischer, D. Slobinsky, and R. S. Perry, Dirac strings and magnetic monopoles in the spin sce $Dy_2Ti_2O_7$, Science **326**, 411 (2009).

[56] J. P. Clancy, J. P. C. Ruff, S. R. Dunsiger, Y. Zhao, H. A. Dabkowska, J. S. Gardner, Y. Qiu, J. R. D. Copley, T. Jenkins, and B. D. Gaulin, Revisiting static and dynamic spin-ice correlations in $Ho_2Ti_2O_7$ with neutron scattering, Phys. Rev. B **79**, 014408 (2009).

[57] P. H. Conlon and J. T. Chalker, Absent pinch points and emergent clusters: Further neighbor interactions in the pyrochlore Heisenberg antiferromagnet, Phys. Rev. B **81**, 224413 (2010).

[58] S. T. Bramwell, M. J. Harris, B. C. den Hertog, M. J. P. Gingras, J. S. Gardner, D. F. McMorrow, A. R. Wildes, A. L. Cornelius, J. D. M. Champion, R. G. Melko, and T. Fennell, Spin Correlations in $Ho_2Ti_2O_7$: A Dipolar Spin Ice System, Phys. Rev. Lett. **87**, 047205 (2001).

[59] B. C. den Hertog, M. J. P. Gingras, S. T. Bramwell, and M. J. Harris, Comment on 'Ising pyrochlore magnets: Low temperature troperties, "ice rules," and beyond' by R. Siddharthan *et al.*, Phys. Rev. Lett. **83**, 1854 (1999), arXiv:cond-mat/9912220.

[60] A. L. Cornelius and J. S. Gardner, Short-range magnetic interactions in the spin-ice compound $Ho_2Ti_2O_7$, Phys. Rev. B **64**, 060406 (2001).

[61] J. Filippi, J. C. Lasjaunias, A. Ravex, F. Tchéou, and J. Rossat-Mignod, Specific heat of dysprosium gallium garnet between 37 mK and 2 K, Solid State Commun. **23**, 613 (1977).

[62] D. C. Mattis and W. P. Wolf, Soluble Extension of the Ising Model, Phys. Rev. Lett. **16**, 899 (1966).

[63] T. Lin, X. Ke, M. Thesberg, P. Schiffer, R. G. Melko, and M. J. P. Gingras, Nonmonotonic residual entropy in diluted spin ice: A comparison between Monte Carlo simulations of diluted dipolar spin ice models and experimental results, Phys. Rev. B **90**, 214433 (2014).

[64] L. Savary and L. Balents, Coulombic Quantum Liquids in Spin-1/2 Pyrochlores, Phys. Rev. Lett. **108**, 037202 (2012).

[65] H. R. Molavian, M. J. P. Gingras, and B. Canals, Dynamically Induced Frustration as a Route to a Quantum Spin Ice State in $Tb_2Ti_2O_7$ via Virtual Crystal Field Excitations and Quantum Many-Body Effects, Phys. Rev. Lett. **98**, 157204 (2007).

[66] S. Onoda and Y. Tanaka, Quantum fluctuations in the effective pseudospin-1/2 model for magnetic pyrochlore oxides, Phys. Rev. B **83**, 094411 (2011).

[67] S. Scharffe, O. Breunig, V. Cho, P. Laschitzky, M. Valldor, J. F. Welter, and T. Lorenz, Suppression of pauling's residual entropy in the dilute spin ice $(Dy_{1-x}Y_x)_2Ti_2O_7$, Phys. Rev. B **92**, 180405 (2015).

[68] R. D. Shannon, Revised effective ionic radii and systematic studies of interatomic distances in halides and chalcogenides, Acta Crystallogr. Sect. A **32**, 751 (1976).

[69] Because of the large crystal-field gap Δ and the strictly Ising nature of the ground doublet of Dy^{3+} in $Dy_2Ti_2O_7$, there are in this material negligible quantum transverse field effects, unlike in the $LiHoF_4$ dipolar Ising ferromagnet. See M. J. P. Gingras and P. Henelius, Collective phenomena in the $LiHo_xY_{1-x}F_4$ quantum Ising magnet: Recent progress and open questions, J. Phys.: Conf. Ser. **320**, 012001 (2011).

[70] Equivalently, this experiment can be done with a so-called "vector magnet" in which one can tune independently a "horizontal" and a "vertical" magnetic field. Such an apparatus was used in the experiment exploring the physics of magnetic ordering in a strong [112] field and reported in Ref. [38].

[71] L. Savary, K. A. Ross, B. D. Gaulin, J. P. C. Ruff, and L. Balents, Order by Quantum Disorder in $Er_2Ti_2O_7$, Phys. Rev. Lett. **109**, 167201 (2012).

[72] K. A. Ross, L. Savary, B. D. Gaulin, and L. Balents, Quantum Excitations in Quantum Spin Ice, Phys. Rev. X **1**, 021002 (2011).

[73] R. Applegate, N. R. Hayre, R. R. P. Singh, T. Lin, A. G. R. Day, and M. J. P. Gingras, Vindication of $Yb_2Ti_2O_7$ as a Model Exchange Quantum Spin Ice, Phys. Rev. Lett. **109**, 097205 (2012).

[74] N. R. Hayre, K. A. Ross, R. Applegate, T. Lin, R. R. P. Singh, B. D. Gaulin, and M. J. P. Gingras, Thermodynamic properties of $Yb_2Ti_2O_7$ pyrochlore as a function of temperature and magnetic field: Validation of a quantum spin ice exchange Hamiltonian, Phys. Rev. B **87**, 184423 (2013).

[75] J. Oitmaa, R. R. P. Singh, B. Javanparast, A. G. R. Day, B. V. Bagheri, and M. J. P. Gingras, Phase transition and thermal order-by-disorder in the pyrochlore antiferromagnet $Er_2Ti_2O_7$: A high-temperature series expansion study, Phys. Rev. B **88**, 220404 (2013).

[76] H. E. Viertiö and A. S. Oja, Interplay of three antiferromagnetic modulations in the nuclear-spin system of copper, Phys. Rev. B **48**, 1062 (1993).

[77] For fixed J_1, tuning J_{3a} and J_{3b} through the constraints of Eq. (4) drives a transition between the two ground states.

[78] A. C. Anderson, B. Holmström, M. Krusius, and G. R. Pickett, Calorimetric investigation of the hyperfine interactions in metallic Nd, Sm, and Dy, Phys. Rev. **183**, 546 (1969).

[79] A. H. Cooke and J. G. Park, Nuclear spins and magnetic moments of ^{161}Dy, ^{163}Dy, ^{171}Yb and ^{173}Yb, Proc. Phys. Soc., London, Sect. A **69**, 282 (1956).

[80] H. H. Wickman and I. Nowik, The hyperfine structure of ^{161}Dy in Dysprosium salts, J. Phys. Chem. Solids **28**, 2099 (1967).

[81] G. Brunhart, H. Postma, D. C. Rorer, V. L. Sailor, and L. Vanneste, Absolute spin assignments of Dy^{161} and Dy^{163} neutron resonances and the hyperfine coupling constants in Dy^{163}, Z. Naturforsch., A: Astrophys., Phys., Physikalisch. Chem. **A26**, 334 (1971).

[82] C. A. Catanese and H. E. Meissner, Magnetic ordering in $Dy(OH)_3$ and $Ho(OH)_3$, Phys. Rev. B **8**, 2060 (1973).